

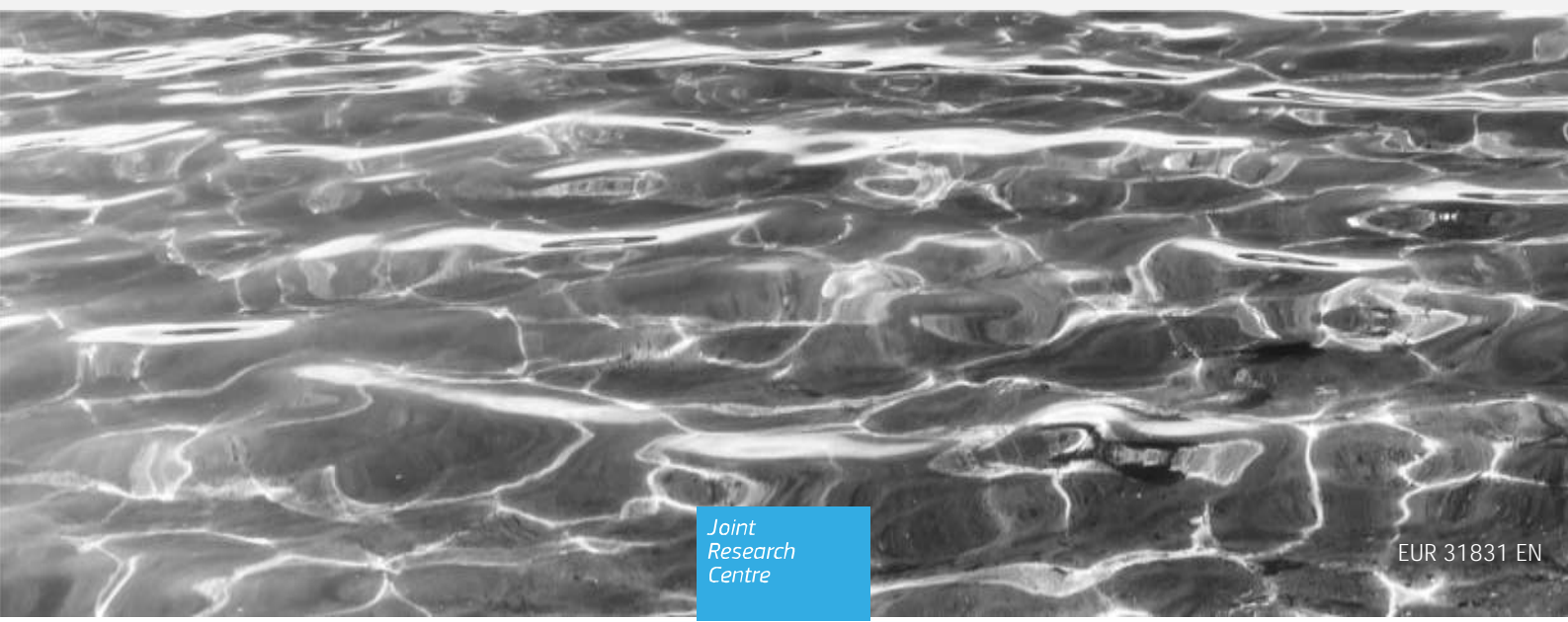


Advanced Radiative Transfer Models for the simulation
of In situ and Satellite Ocean Color data
(ARTEMIS-OC):

the Finite Element Method (FEM)
numerical code

Bulgarelli, B.

2024



This document is a publication by the Joint Research Centre (JRC), the European Commission's science and knowledge service. It aims to provide evidence-based scientific support to the European policymaking process. The contents of this publication do not necessarily reflect the position or opinion of the European Commission. Neither the European Commission nor any person acting on behalf of the Commission is responsible for the use that might be made of this publication. For information on the methodology and quality underlying the data used in this publication for which the source is neither Eurostat nor other Commission services, users should contact the referenced source. The designations employed and the presentation of material on the maps do not imply the expression of any opinion whatsoever on the part of the European Union concerning the legal status of any country, territory, city or area or of its authorities, or concerning the delimitation of its frontiers or boundaries.

Contact information

Name: Barbara Bulgarelli

Address: JRC-EC (Ispra, I)

Email: [barbara.bulgarelli\(at\)jrc.ec.europa.eu](mailto:barbara.bulgarelli(at)jrc.ec.europa.eu)

EU Science Hub

<https://joint-research-centre.ec.europa.eu>

JRC135763

EUR 31831 EN

Print ISBN 978-92-68-12036-1 ISSN 1018-5593 doi:10.2760/37453

KJ-NA-31-831-EN-C

PDF ISBN 978-92-68-12037-8 ISSN 1831-9424 doi:10.2760/30247

KJ-NA-31-831-EN-N

Luxembourg: Publications Office of the European Union, 2024

© European Union, 2024



The reuse policy of the European Commission documents is implemented by the Commission Decision 2011/833/EU of 12 December 2011 on the reuse of Commission documents (OJ L 330, 14.12.2011, p. 39). Unless otherwise noted, the reuse of this document is authorised under the Creative Commons Attribution 4.0 International (CC BY 4.0) licence (<https://creativecommons.org/licenses/by/4.0/>). This means that reuse is allowed provided appropriate credit is given and any changes are indicated.

For any use or reproduction of photos or other material that is not owned by the European Union permission must be sought directly from the copyright holders.

How to cite this report: European Commission, Joint Research Centre, Bulgarelli, B., Advanced Radiative Transfer Models for the simulation of In situ and Satellite Ocean Color data (ARTEMIS-OC): the Finite Element Method (FEM) numerical code, Publications Office of the European Union, Luxembourg, 2024, <https://data.europa.eu/doi/10.2760/30247>, JRC135763.

Contents

Abstract	2
Foreword.....	3
Acknowledgements	5
1 Introduction	6
1.1 ARTEMIS-OC.....	8
2 Basic Principles.....	12
2.1 The Radiance	12
2.2 The Radiative Transfer Equation	13
3 The FEM numerical code	15
3.1 Applied methodology	15
3.2 Inputs and Outputs	16
3.3 FEM code accuracy	24
4 FEM code validation	25
4.1 Benchmark with data from the literature.....	25
4.2 Benchmark with the MC code by Roberti (1997).....	25
4.3 Benchmark with the PHO-TRAN code	26
4.4 Benchmark with the NAUSICAA code	28
4.5 Benchmark with Hydrolight	29
4.6 Benchmark with experimental <i>in situ</i> data.....	29
5 FEM code applications.....	30
5.1 Simulation of the signal at satellite sensors in support to the processing and accuracy assessment of satellite data	30
5.2 Simulation of the in-water light field in support to the development of bio-optical algorithms.....	31
5.3 Simulation of the sky-radiance distribution in support to the assessment and minimization of uncertainties in <i>in situ</i> data	32
6 Conclusions.....	34
References.....	36
List of abbreviations and definitions	39
List of figures.....	40
List of tables.....	42
Annexes	43
Annex 1. Code Structure	43
Annex 2. Input-files format	43
Annex 3. Output-files format	47
Annex 4. Accuracy of the solution	49
Annex 5. Compilation and linking	49
Annex 6. Program Parameters	50
Annex 7. Program Main Variables	51

Abstract

The present Report, first of a series, builds on JRC long-standing experience in developing and applying highly accurate *radiative transfer models* (RTMs) to simulate *in situ* and satellite data of the aquatic environment.

In-house modelling capabilities of the signal at *in situ* and satellite OC sensors, included in the Advanced Radiative Transfer Models for In situ and Satellite Ocean Color data (ARTEMIS-OC) software suite, comprise: i) the Finite Element Method code (FEM); ii) the SkyFEM code; iii) the FEMrad-OC code; iv) the AquaFEM code; v) the Novel Adjacency Perturbation Simulator for Coastal Areas (NAUSICAA) code.

FEM is a highly accurate deterministic numerical scheme for the propagation of unpolarized solar radiation in a horizontally invariant atmosphere-water system, as the open-ocean. NAUSICAA is a stochastic 3D MonteCarlo code for the propagation of unpolarized solar radiation in an atmosphere bounded by an inhomogeneous surface, as in coastal or inland water regions. SkyFEM, FEMrad-OC and AquaFEM are FEM targeted configurations coupled with ad-hoc modelling of atmosphere and water.

All algorithms account for multiple scattering and allow varying illumination and observation geometries.

The present Report illustrates the FEM code and summarizes a number of applications to investigate and reduce uncertainties in OC products.

The final objective of this series of Reports is to consolidate the description of ARTEMIS-OC simulation tools in support of the Copernicus Programme.

Foreword

The Copernicus Programme established by the European Union in 2014 (Regulation EU No377/2014) aims at creating a European capacity for Earth Observation (EO). This is achieved by developing user and policy driven information services with a long-term commitment to provide full, free and open access to EO satellite and *in situ* data.

As such, the Copernicus Programme plays an essential role in the monitoring of the implementation of the European Climate Law, which is a key-initiative of the European Green Deal.

Among the several Copernicus specific services, the Copernicus Marine Environment Monitoring Service (CMEMS) and the marine component of the Climate Change Service (C3S) both rely on EO data derived from satellite ocean color (OC) sensor measurements, such as the radiance L_w leaving water bodies or the derived Chlorophyll-a concentration used as a proxy for phytoplankton biomass.

OC data products are relevant to evaluate ocean ecosystem health and productivity, to assess the role of the oceans in the global carbon cycle, to manage living marine resources, and to quantify the impact of climate variability and change. They have been indeed identified by the Global Ocean Observing System (GOOS) as Essential Ocean Variables (EOV) to monitor the health of the oceans, and by the Global Climate Observation System (GCOS) as Essential Climate Variable (ECV) to support the work of the United Nations Framework Convention on Climate Change (UNFCCC).

To ensure a maximized return of investment for the Copernicus Programme, the fitness-for-purpose of OC products for environmental and climate application must be accurately assessed. This implies a thorough evaluation of the uncertainties affecting satellite and *in situ* data, as well as the procedures applied for the retrieval of OC data products from the satellite observations.

Modelling techniques to theoretically simulate the global signal at *in situ* and satellite sensors, as well as its distinct components, are powerful tools for the evaluation of uncertainties affecting data products. Modelling indeed provides the most logical linkage between observations and physical processes, thus uniquely allowing individuating and separately analysing the different sources of perturbations affecting satellite and *in situ* data.

The present Report, first of a series, summarizes the multi-decennial JRC effort in the development and application of highly accurate numerical models for the simulation of OC satellite and *in situ* data, by introducing the JRC in-house suite of Advanced Radiative Transfer Models for In situ and Satellite Ocean Color data (ARTEMIS-OC), which includes:

- The Finite Element Method radiative transfer code (FEM), conceived to simulate the propagation of the solar radiation in a layered medium with a change in the refractive index (like the atmosphere-ocean system);
- The SkyFEM code designed to simulate the sky-radiance distribution;
- The FEMrad-OC code for a comprehensive simulation of the signal received by satellite OC sensors;
- The AquaFEM code allowing to simulate radiance distribution and the apparent optical properties within and just above any natural water body;
- The Novel Adjacency Perturbation Simulator for Coastal Areas (NAUSICAA), implemented to investigate perturbations induced by nearby land surfaces in OC data from coastal or inland waters;

While FEM is a one-dimensional deterministic numerical code, NAUSICAA is a stochastic three-dimensional numerical code. SkyFEM, FEMrad-OC and AquaFEM are targeted configurations of the FEM code coupled with ad-hoc modelling of atmosphere and water.

ARTEMIS-OC models accomplish the five principles set out in the manifesto for best practices for responsible mathematical modelling (Saltelli et al., 2020): they all mind the assumptions, the hubris, the framing, the consequences, and the unknowns.

The present report describes the FEM radiative transfer code.

The FEM numerical code has been extensively applied over the years to support the calibration and validation of Earth Observation (EO) missions, and for the analysis of uncertainties affecting *in situ* and satellite data products.

FEM simulations are also operationally utilized for the processing of EO data.

Specifically, the FEM code has been employed to build the radiative transfer database included in the Modular Inversion and Processing System (MIP) (Heege et al., 2014) (Kiselev et al., 2015): an operational processor supporting the analysis of marine and inland water remote sensing data from the high-resolution Environmental Mapping and Analysis Program (EnMAP) (Storch et al., 2023) successfully launched in 2022.

MIP also serves as data processor for the World Water Quality Portal, conceptualized and developed in the framework of the International Initiative on Water Quality (IIWQ) of the Intergovernmental Hydrological Programme (IHP) of the United Nations Educational, Scientific and Cultural Organization (UNESCO). It showcases and demonstrates the potential of remote sensing and satellite Earth Observation for the improvement of water quality monitoring towards sustainable water resources management (IIWQ, 2018)

Acknowledgements

The content of this Report summarizes results published in peer-review literature by the same author in collaboration with a number of colleagues whose contribution is duly acknowledged. Specifically, grateful thanks are due to: dr. Viatcheslav Kiselev, former EOMAP GmbH and Co., dr. Giuseppe Zibordi (NASA GSFC & University of Maryland Baltimore County, former JRC), and dr. J-F. Berthon (JRC).

This Report is a contribution to *Fiducial Ocean and Land Earth Observations* (FOLEO) funded by the Joint Research Centre (JRC).

The support provided by DG DEFIS (the European Commission Directorate-General for Defence Industry and Space) and the Copernicus Programme is also gratefully acknowledged.

Authors

Barbara Bulgarelli, EC-JRC, Ispra (VA) - I

1 Introduction

"Look deep into nature, and then you will understand everything better"
Albert Einstein

After having travelled undisturbed through the empty space for about 149.6 million km, the light emitted by the Sun enters the Earth atmosphere, where it begins to interact with molecules and aerosol particles. Some light is absorbed; other is scattered. Diffuse and direct sunlight might reach the land and be absorbed or scattered again. Or it might reach the surface of the sea, where it is partly reflected back to the air, and partly transmitted to the water body. Within the water, the light might interact with water molecules and other optically active components (like pigmented particles, sediments, color dissolved organic matter) and eventually reach the sea bottom.

At each stage of its interaction with the Earth's environment, sunlight might be eventually diffused into the aperture of an observing sensor. This light detected by the sensor encrypts a phenomenal wage of information on the environment it interacted with.

Accurately decrypting the message carried by the light is the scientific challenge of optical remote sensing.

Radiative transfer models (RTMs) represent a fundamental mean to decipher the information collected by satellite and *in situ* sensors, and to assess the quality of the derived data products. Indeed, by theoretically replicating the journey of the solar radiation within the Earth environment and up to the optical sensor, RTMs provide the most logical linkage between observations and physical processes.

The capability of RTMs to theoretically quantify the different radiance contributions at the sensor, further allows a comprehensive investigation of the perturbations affecting field and satellite measurements, thus supporting the development, implementation, assessment and refinement of correction schemes and protocols for satellite and *in situ* measurements.

Any RTM can be thought as the combination of a core algorithm for the solution of the mathematical equation describing the transferring of the radiation (the so-called *radiative transfer equation*, RTE) with a parametric modelling of the system in which the radiance propagates (i.e., the *propagating system*) (see Fig. 1).

The accuracy of the RTM hence relies on a correct, accurate and efficient mathematical solution of the RTE, and a correct and accurate characterization of the system in which the radiance propagates.

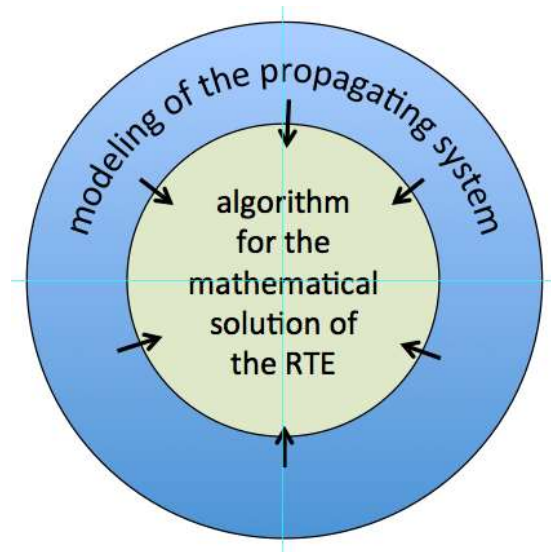
The most accurate numerical method for the solution of the RTE will never provide a realistic description of the actual light field if input parameters and boundary conditions do not properly describe the system in which the radiance propagates.

Similarly, the most accurate modelling of the propagating system will never lead to an accurate description of the radiance field if the mathematical solution of the RTE does not properly account for the relevant physical processes.

RTM fit-for-purpose relies on the coupling of an accurate modelling of the propagating system and an accurate mathematical treatment of the RTE.

Last but not least, a significant role is also played by the interface between user and RTM, which can vary from a rather simplistic one letting the user define every input of the RTE, to a more sophisticated one requiring fewer definitions by the user.

Figure 1. Scheme of a RTM, as composed by a core algorithm for the mathematical solution of the RTE and a parametric modelling of the propagating system

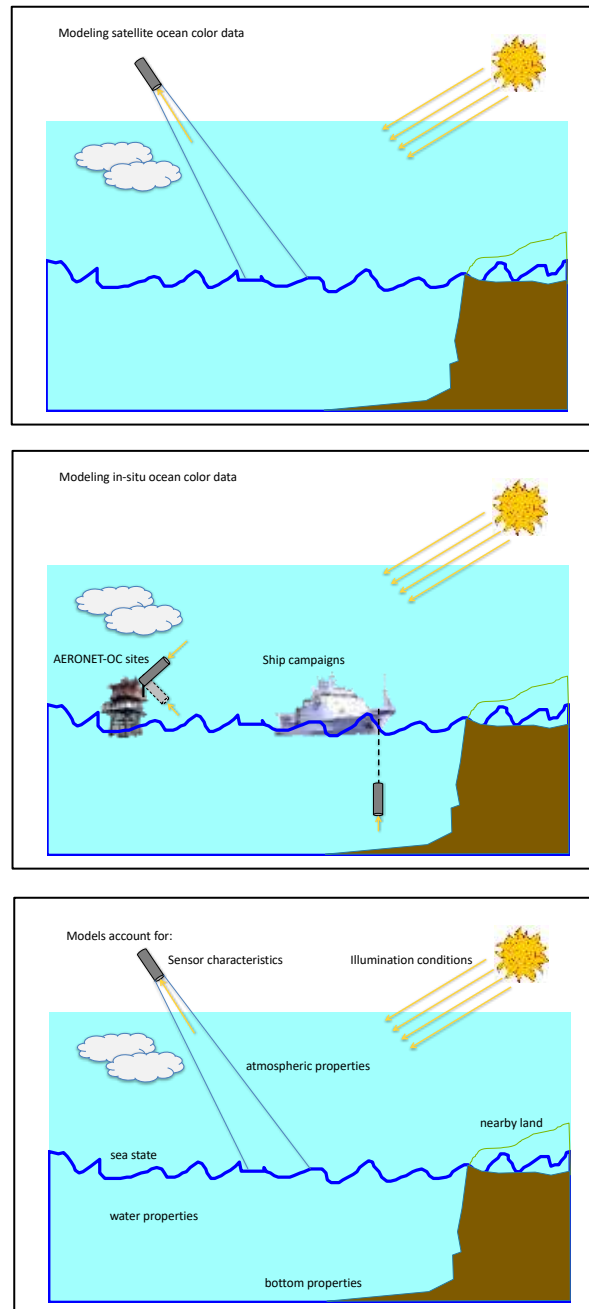


Source: JRC, 2024

1.1 ARTEMIS-OC

The Advanced Radiative Transfer Models for In situ and Satellite Ocean Color data (ARTEMIS-OC) includes different RTMs offering the capability to simulate the different components of the total unpolarized radiance received by satellite or *in situ* OC sensors at any visible and near-infrared (NIR) center-wavelength, and for any illumination and observation geometry (see Fig. 2).

Figure 2. ARTEMIS-OC modelling capabilities



Source: JRC, 2024

The ARTEMIS-OC software suite, comprises:

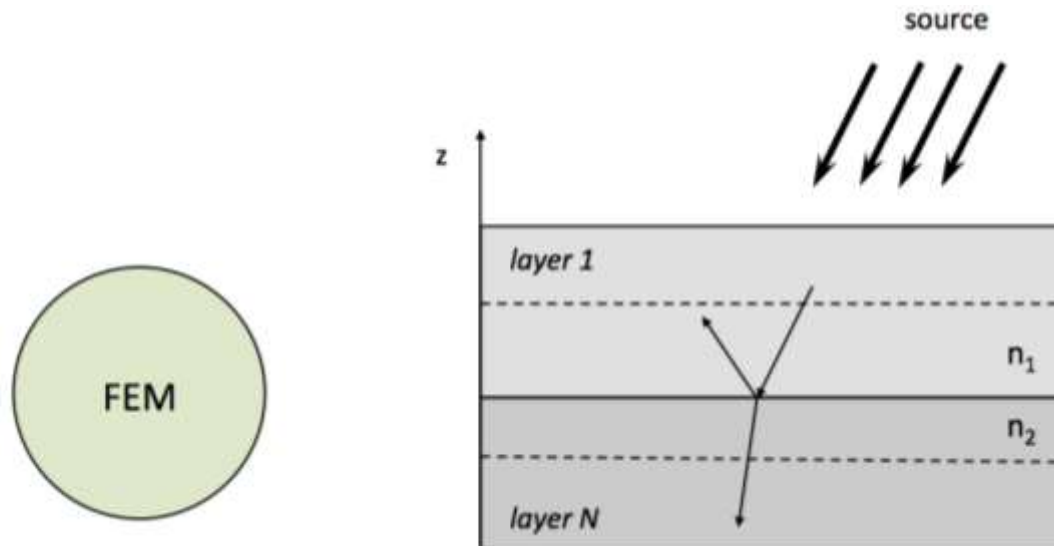
- The Finite Element Method radiative transfer code (FEM), designed to simulate the propagation of the unpolarized solar radiation in a layered medium with a change in the refractive index (like the atmosphere-ocean system) (Bulgarelli et al., 1999)
- The SkyFEM code allowing to simulate the sky-radiance distribution;
- The FEMrad-OC code for the simulation of the signal received by satellite ocean color sensors;
- The AquaFEM code for simulating radiance distributions and apparent optical properties within and just above any natural water body;
- The Novel Adjacency Perturbation Simulator for Coastal Areas (NAUSICAA), to investigate adjacency perturbations induced by nearby land in OC data from coastal regions or inland water basins (Bulgarelli et al., 2014).

The FEM code (Bulgarelli et al., 1999) implements a highly accurate deterministic numerical algorithm based on the finite element method to simulate the propagation of unpolarized solar radiation in a system with horizontally invariant optical properties and presenting a change in the refractive index (Fig. 3), as in open-ocean observations.

SkyFEM, FEMrad-OC and AquaFEM are targeted configurations of the FEM code coupled with an ad-hoc modelling of atmosphere and water (Fig. 4 and 5).

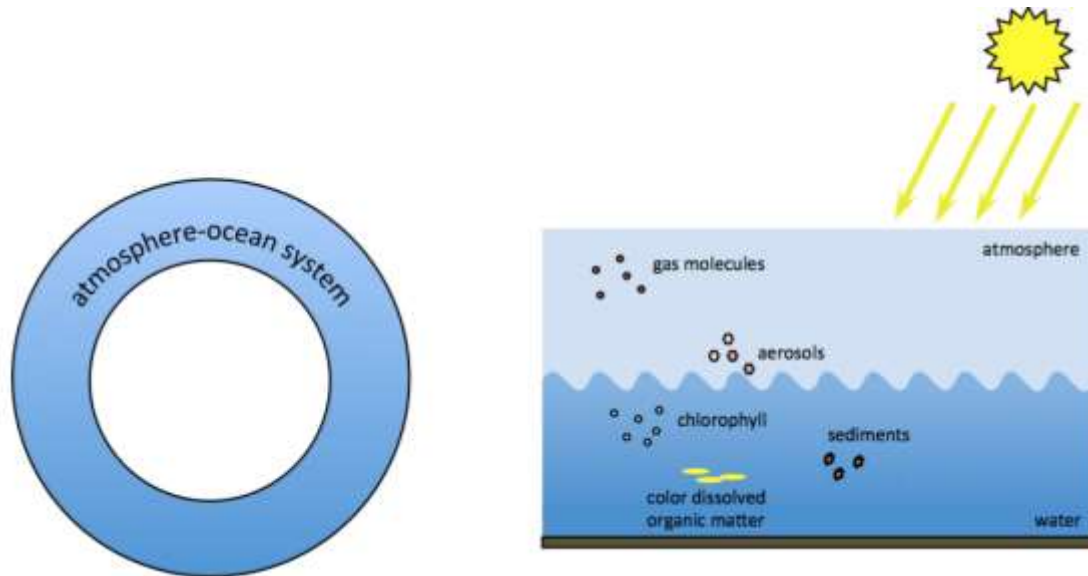
NAUSICAA (Bulgarelli et al., 2014) is a stochastic three-dimensional (3D) MonteCarlo (MC) code for the propagation of the unpolarized solar radiation in an atmospheric medium bounded by an inhomogeneous reflecting surface (Fig 6), as it occurs in coastal or inland regions.

Figure 3. Scheme of the FEM code for the solution of the RTE



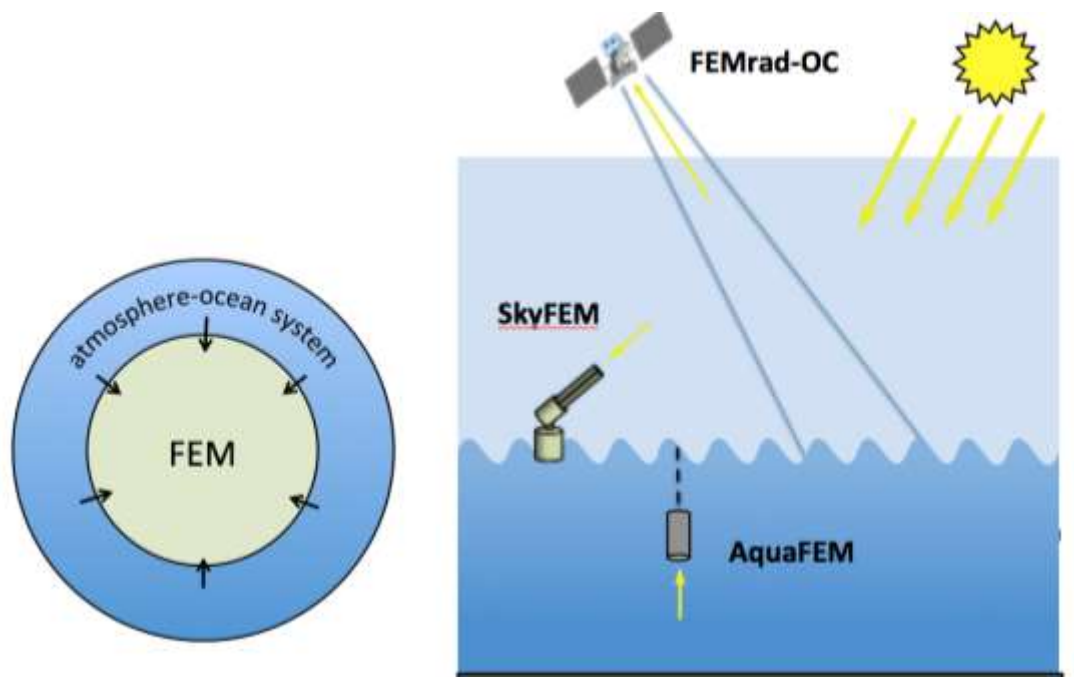
Source: JRC, 2024

Figure 4. Scheme for the modelling of the propagating system



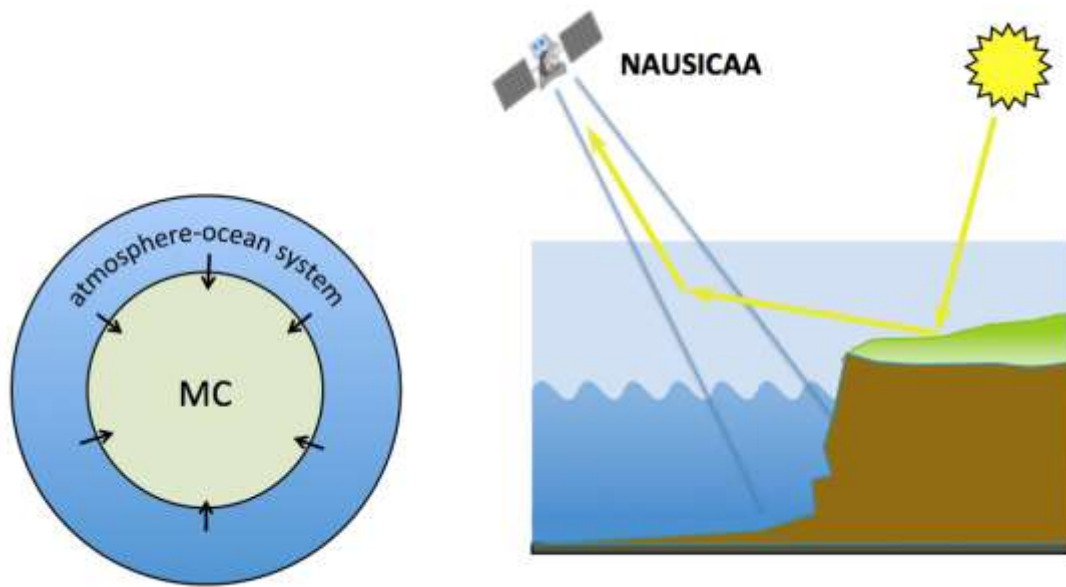
Source: JRC, 2024

Figure 5. Scheme for SkyFEM, FEMrad-OC and AquaFEM



Source: JRC, 2024

Figure 6. Scheme for NAUSICAA



Source: JRC, 2024

All algorithms account for multiple interactions within the propagating system and allow considering varying illumination and observation geometries.

Ultimately, ARTEMIS-OC guarantees efficient and accurate in-house capabilities to model the radiance contributions received by OC satellite and *in situ* sensors operating in oceanic, coastal and inland waters. ARTEMIS-OC is indeed able to provide the most efficient treatment of the RTE for sunlight propagation in horizontally optically homogeneous systems, while, when appropriate, it ensures the capability to account for variations in the optical properties of the reflecting surface.

The present report focuses on the description of the FEM numerical code, which represents an accurate and powerful tool for the numerical solution of the RTE in a layered medium characterized by one change in the refractive index.

Section 2 provides a short definition of the radiance and a brief description of the RTE. Section 3 illustrates the FEM code, including implemented mathematical method, code accuracy and structure, as well as inputs and outputs description. Results from the extensive validation of the FEM code are presented in Section 4. Most relevant FEM applications are summarized in Section 5. Conclusions are drawn in Section 6.

2 Basic Principles

Ocean color remote sensing involves the measurement of the electromagnetic radiation that has been reflected by the ocean at near ultraviolet (UV, ~ 300 to 380 nm), visible (VIS, 380 to 780 nm) and near-infrared (NIR, 780 to less than 2000 nm) wavelengths, the so-called *optical wavelengths*, with the Sun being the only source: a parallel beam of irradiance F_0 hitting the top-of-the-atmosphere (TOA).

In principle, by solving Maxwell's equations with the appropriate boundary conditions, it is possible to determine the propagation of electromagnetic energy under any given set of circumstances. In practice this is quite challenging, except for the simplest cases.

For what concerns the transferring of solar electromagnetic radiation in the atmosphere-water system, the *light* is primarily seen as a carrier of energy, and a description of the transfer of energy is sought. The Sun is in fact a natural source, emitting incoherent radiation, interacting with randomly distributed particles, different in geometrical and physical properties.

The basic quantity is not the electromagnetic field, but the *radiance*, which is a quantity strictly related to the energy associated to the electromagnetic radiation.

Radiometry is the science of measuring light in any portion of the electromagnetic spectrum, while radiance propagation in a media characterized by absorbing, emitting and scattering processes is described by the *Radiative Transfer Equation* (RTE).

Sections 2.1 and 2.2 will illustrate the basic concepts of radiometry and radiative transfer.

2.1 The Radiance

When the radiation is continuously distributed over the spectrum, and its variation over the spectrum is accounted for, its quantity in the neighbourhood of any particular wavelength depends on the width of the neighbourhood. As the neighbourhood becomes infinitesimal, the amount of radiation itself becomes infinitesimal and proportional to this width. In such case the ratio

$$\lim_{\Delta\lambda \rightarrow 0} \frac{Q(\lambda_0, \lambda_0 + \Delta\lambda)}{\Delta\lambda} = Q_{\lambda_0} \quad (1)$$

has a definite limit called the spectral density of the quantity (in literature the *spectral* or *monochromatic quantity*), which is useful in describing the spectral distribution of the quantity. In the following parts of the report, all quantities will be spectral.

The basic quantity in radiometry is the radiant energy traversing a surface in the unit time: the *radiant flux* Φ_λ .

The differential amount of spectral radiant flux $d\Phi_\lambda$ crossing an element of area dA (see Fig. 7) in a direction confined to a differential solid angle (oriented at an angle θ to the normal to dA) may be expressed in terms of the *radiance* L_λ as

$$d\Phi_\lambda = L_\lambda \cos\theta d\Omega dA d\lambda \quad (2)$$

where $d\Omega = \sin\theta d\theta d\phi$.

Eq. (2) defines the spectral radiance in general terms as

$$L_\lambda = \frac{d\Phi_\lambda}{\cos\theta d\Omega dA d\lambda} \quad , \quad (3)$$

generally expressed in units of $\text{Wm}^{-2}\mu\text{m}^{-1}\text{sr}^{-1}$.

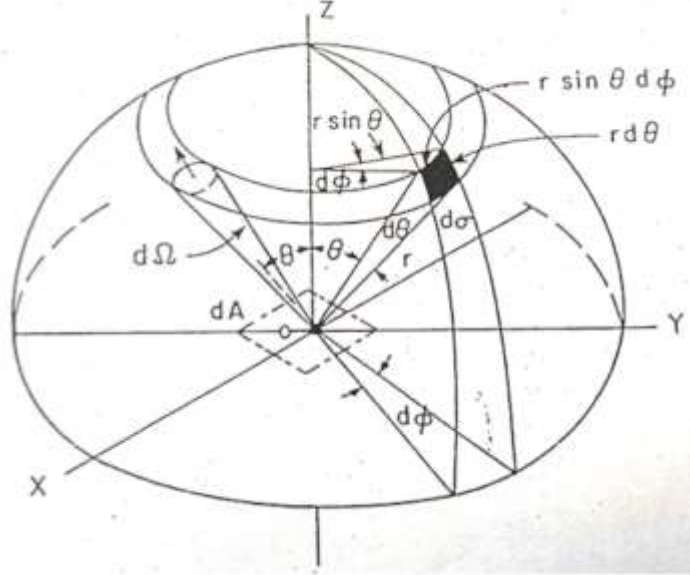
Clearly the radiance implies a directionality in the radiation stream; because of this the radiance is commonly said to be confined in a *pencil of radiation*.

In a generic radiation field, the radiance may be expected to vary not only from point to point but also with direction through every point. Thus, for a general radiation field, we may write

$$L_\lambda \equiv L(\vec{r}; \hat{\xi}; \lambda) \quad (4)$$

where the position vector \vec{r} is of Cartesian coordinates (x, y, z) ; and the direction unit vector $\hat{\xi}$ is expressed in terms of the zenith angle θ and the azimuth angle ϕ (see Fig. 7).

Figure 7. Illustration of a solid angle and its representation in polar coordinates. Also shown is a pencil of radiation through an element of area dA in directions confined to an element solid angle $d\Omega$.



Source: Bulgarelli, PhD dissertation, 1998

The *spectral irradiance* is defined by the normal component of L_λ integrated over the entire spherical solid angle, and it is commonly written as

$$E_\lambda \equiv \int_\Omega L_\lambda \cos\theta d\Omega = \int_0^{2\pi} \int_0^\pi L_\lambda \cos\theta \sin\theta d\theta d\phi, \quad (5)$$

generally expressed on units of $\text{Wm}^{-2}\mu\text{m}^{-1}$.

It is noted that the irradiance E is dimensionally identical with the electromagnetic *intensity* of an electromagnetic wave, i.e., the time-average of the *Poynting vector* \vec{S} , which represents the flow of electromagnetic energy across a unit area element (normal to \vec{S}) per unit time.

2.2 The Radiative Transfer Equation

The radiative transfer equation (RTE) mathematically describes the propagation of the radiance L at the wavelength λ from position \vec{r} in direction $\hat{\xi}$ through an absorbing, emitting and scattering medium

$$(\hat{\xi} \cdot \nabla)L(\vec{r}; \hat{\xi}; \lambda) = -c(\vec{r}; \lambda)L(\vec{r}; \hat{\xi}; \lambda) + \int_\Omega L(\vec{r}; \hat{\xi}'; \lambda)\beta(\vec{r}; \hat{\xi}' \rightarrow \hat{\xi}; \lambda)d\Omega' + S(\vec{r}; \hat{\xi}; \lambda) \quad (6)$$

where ∇ is the gradient operator; $c(\vec{r})$ is the attenuation coefficient at \vec{r} ; β is the Volume Scattering Function (VSF) describing the angular distribution at \vec{r} of the scattered radiation with respect to $\hat{\xi}$; and $S(\vec{r}; \hat{\xi})$ is the source term.

In the following, the spectral dependence will be omitted for simplicity of notation.

Eq. (6) describes the variation of the radiance L per unit distance along $\hat{\xi}$: the first additive term on the right represents the radiance loss at \vec{r} along $\hat{\xi}$ due to attenuation; the integral term describes the radiance gain due to the scattering at \vec{r} in direction $\hat{\xi}$ of radiance originating from any direction $\hat{\xi}'$; and the last additive term designates the emission from the source S .

By recalling that the attenuation coefficient is the sum of the absorption $a(\vec{r})$ and scattering $b(\vec{r})$ coefficients, $c(\vec{r}) = a(\vec{r}) + b(\vec{r})$, and that $b(\vec{r}) = \int_{4\pi} \beta(\vec{r}; \hat{\xi}' \rightarrow \hat{\xi})d\Omega'$, Eq. (6) becomes

$$\frac{(\hat{\xi} \cdot \nabla) L(\vec{r}; \hat{\xi})}{c(\vec{r})} = -L(\vec{r}; \hat{\xi}) + \omega_0(\vec{r}) \int_{\Omega} L(\vec{r}; \hat{\xi}') \tilde{\beta}(\vec{r}; \hat{\xi}' \rightarrow \hat{\xi}) d\Omega' + \tilde{S}(\vec{r}; \hat{\xi}) \quad (7)$$

where $\omega_0 = b/c$ is the single scattering albedo (describing the ratio of scattering efficiency to total extinction efficiency); $\tilde{\beta} = \beta/b$ is the scattering phase function defining the probability that radiance at \vec{r} from any direction $\hat{\xi}'$ is scattered into direction $\hat{\xi}$; and $\tilde{S} = S/c$.

Analytical solutions of the RTE are only possible under restrictive assumptions, and most realistic OC studies require a numerical approach, be either deterministic or stochastic.

Deterministic methods are computationally extremely efficient and are free from statistical uncertainties; yet, they tend to be mathematically complex, physically non-direct and so generally unfitted for complex 3D geometries.

Stochastic methods, based on MC photon-transport algorithms, are physically direct, mathematically simpler; yet computationally demanding and affected by statistical uncertainties.

While the supremacy of MC method becomes unquestionable when 3D geometries and/or time-dependent problems are involved, highly accurate and efficient deterministic solutions are better suited in cases of horizontally translational invariance (i.e., plane-parallel systems).

Whichever the numerical methodology applied, the solution of Eq. (7) requires the knowledge of the parameters c , ω_0 and $\tilde{\beta}$ [equivalent to parameters c and β , in Eq. (6)], and of the boundary conditions. In other words, it requires a description of the propagating system.

3 The FEM numerical code

The Finite Element Method radiative transfer code (FEM) represents an accurate and powerful tool for the numerical solution of the RTE in a generic layered medium characterized by a change in the refractive index. It applies the finite element deterministic approach to model the propagation of unpolarized monochromatic radiation in the ultraviolet, visible and near-infrared electromagnetic regions within a vertically inhomogeneous system with a change in the refractive index and bounded by a reflecting surface (see Fig. 3), like the atmosphere-ocean system.

The code assumes a smooth air-water interface (which is acceptable for wind speeds up to the Beaufort velocity (Monahan and O'Muircheartaigh, 1986) and does not account for inelastic scattering phenomena, such as Raman scattering and fluorescence.

The solution can be simultaneously computed at different heights within the medium and for different directions of propagation.

Sections 3.1 to 3.4 provide a general illustration of the FEM code, including the description of the applied methodology, FEM inputs and outputs, and FEM accuracy.

FEM code structure and memory requirements are presented in Appendix A.

3.1 Applied methodology

A concise description of the mathematical methodology implemented in FEM is here provided. The reader is addressed to (Bulgarelli et al., 1999; Kisselev et al., 1995) for additional details.

By dividing the atmosphere-ocean system into a suitable number \mathcal{L} of optically homogeneous horizontal layers, the RTE for the plane-parallel system becomes:

$$\eta \frac{dL(\tau; \eta, \phi)}{d\tau} = -L(\tau; \eta, \phi) + \frac{\omega_{0l}}{2} \int_{4\pi} L(\tau; \eta', \phi') \tilde{\beta}_l(\tau; \eta', \phi' \rightarrow \eta, \phi) d\Omega' + \tilde{S}_l(\tau, \eta) \quad (8)$$

where l is the layer index ($l = 1, \dots, \mathcal{L}$), $\tau = \int c(z) dz$, and $\eta = \cos \theta$.

The phase function $\tilde{\beta}$ is expanded into a series of Legendre polynomials P_k with an appropriate finite number of terms M to decouple the dependence on the azimuth ϕ

$$\tilde{\beta}(\tau; \cos \theta) = \sum_{k=0}^M x_k P_k(\cos \theta) \quad (9)$$

where x_k are the Legendre coefficients (alternatively called Legendre moments).

By recalling that

$$\cos \theta = \eta \eta' + \sqrt{1 - \eta^2} \sqrt{1 - \eta'^2} \cos(\phi' - \phi), \quad (10)$$

and by making use of the associated Legendre polynomials P_k^m and of the addition theorem for spherical harmonics (Liou, 2002), Eq. (9) can be rewritten as

$$\sum_{m=0}^M p^m(\eta, \eta') \cos m(\phi' - \phi) = \sum_{m=0}^M \sum_{k=m}^M x_k^m P_k^m(\eta) P_k^m(\eta') \cos m(\phi' - \phi) \quad (11)$$

where

$$x_k^m = (2 - \delta_{0,m}) x_k \frac{(k-m)!}{(k+m)!}, \quad (12)$$

with $\delta_{0,m} = 0(1)$ for $m = 0(m \neq 0)$.

The radiance L is correspondingly expanded in a Fourier cosine series

$$L(\tau; \eta, \phi) = \sum_{m=0}^M L^m(\tau, \eta) \cos m\phi, \quad (13)$$

where $L^m(\tau, \eta)$ represents the m -th radiance harmonic.

This enables the analytical integration of Eq. (8) with respect to ϕ , and its separation into $M+1$ independent equations. The resulting equation for the m -th Fourier radiance component of the l -th layer becomes

$$\eta \frac{dL^m(\tau; \eta)}{d\tau} = -L^m(\tau; \eta) + \frac{\omega_{0l}}{2} \int_{-1}^1 L^m(\tau; \eta') p^m(\tau; \eta, \eta') d\eta' + Q_l^m(\tau, \eta), \quad (14)$$

where Q_l^m indicates the source functions, whose expression differs between atmosphere and water.

The remaining integrals are further approximated by projecting each radiance harmonic L^m onto a set of basis functions, each different from zero only in a finite interval (hence, the "finite element" designation of this method).

Specifically, the solution of Eq. (14) is sought in the form

$$L^m(\tau, \eta) = \sum_{i=1}^{2N} L_i^m(\tau) b_i^m(\eta) \quad (15)$$

with

$$b_i^m(\eta) = Y_m^m(\eta) \begin{cases} 1 - \frac{|\eta - \eta_i|}{h} & \text{if } |\eta - \eta_i| < h \\ 0 & \text{elsewhere} \end{cases} \quad (16)$$

In Eq. (16) Y_m^m are the spherical harmonics, η_i ($i = 1, \dots, 2N$) are the nodes of the homogeneous grid in the interval $[-1, 1]$, and $h = 1/(N - 1)$ is the grid step.

The resulting system of matricial equations is solved analytically, imposing the necessary boundary conditions, i.e., zero radiance at the top of the atmosphere; continuity of the solution at the boundaries between sub-layers; Fresnel reflection and transmission at the boundary with a change in the refractive index; bottom Lambertian reflectance.

The solutions are finally improved by applying an interpolation procedure.

FEM ensures flux conservation independently of the number of grid points ($N=2$ is already sufficient) and of the shape of the phase function (i.e., of the order of polynomials M used to correctly represent it), opposite to alternative numerical methods (e.g., the Discrete Ordinate Method), which requires that the number of Gaussian quadrature points N used to solve the RTE integral is at least equal to the number of Legendre polynomials M . Additionally, by selecting basis functions which are finite, FEM generates a piecewise approximate solution that may converge faster than other global approximations (e.g., those adopted in the Spherical Harmonic Method). A number of grid points $N=64$ is usually sufficient to accurately model the radiance angular distribution even when characterized by extreme variations.

The approach implemented in FEM is thus particularly suitable for highly asymmetric phase functions, like those characterizing the scattering by aerosols and hydrosols.

3.2 Inputs and Outputs

In the following, an atmosphere-ocean system is assumed, since it represents the main FEM application; nonetheless, any system with a change in the refractive index might be analogously defined.

A leading input file, called MAIN.DAT (whose name needs to remain unchanged) must include the names of *i)* the input file defining the characteristics of the propagating medium (e.g., *card1.dat*); *ii)* the input file defining the output characteristics (e.g., *card2.dat*); *iii)* the name of the uncommented output file (e.g., *ofname.dat*); *iv)* the name of the verbose output file (e.g., *ofname.out*); and *v)* the name of the file containing the Legendre moments of the phase function, when not determined through a parametric equation (e.g., *momname.dat*).

An example of MAIN.DAT is provided in Fig. 8. The detailed description of the format of all input files is given in Appendix A.2.

Figure 8. Example of MAIN.DAT input file.

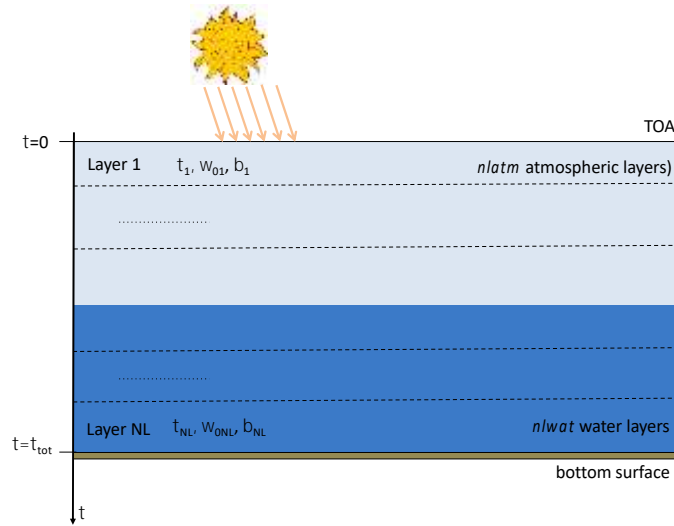
Example of FEM input card	
Input File:	card1.dat
Output Characteristic:	card2.dat
Output File1:	ofname.dat
Output File2:	ofname.out
Henyey-Greenstein:	1
Phasefunction file:	rayleigh.dat

Source: JRC, 2024

Definition of the propagating system

The definition of the propagating system (see Fig. 9) must include information on the illumination conditions, on the optical properties of atmosphere and water layers, and on the bottom surface. An example of the input file defining the characteristics of the propagating medium (e.g., *card1.dat*) is provided in Fig. 10.

Figure 9. Scheme of the atmosphere-ocean system



Source: JRC, 2024

The incident radiation (a parallel flux impinging on the top boundary) is defined through the solar zenith angle (i.e., the angle in degrees between the incident beam direction and the normal to the surface) and the solar spectral irradiance at the top of the atmosphere (on a surface normal to the solar beam direction).

The atmosphere-ocean system is divided into plane-parallel layers of uniform optical properties, and the number of optically homogeneous atmospheric and water layers, as well as their refractive index, must be indicated.

For each layer the optical thickness τ , the single scattering albedo ω_0 , and the scattering phase function are required.

Figure 10. Example of input file defining the characteristics of the propagating medium (e.g., *card1.dat*).

SYSTEM CHARACTERISTICS			
Number of grid points (half interval)		4	
Solar Zenith Angle (deg) 50.0000		Solar Spectral Irradiance at the Top 1.0	
Underlying Surface:		Albedo 0.5000	Asymm. Factor 0.0000
Atmosphere-Ocean System:		#layers	Refractive Index
atm		2	1.0000
wat		2	1.3410
# Layers Characteristics:			
layer nr.	ssa	tau	
1	0.750000000	0.400000000	
2	0.800000000	0.200000000	
3	0.850000000	8.500000000	
4	0.600000000	7.500000000	
# if Henyey-Greenstein Phase Function [if STHG g2(j)=0.d0 and as(j)=1.d0]			
layer nr.	g1	g2	as
1	0.500000000	0.400000000	0.500000000
2	0.600000000	0.500000000	0.800000000
3	0.900000000	0.700000000	0.950000000
4	0.200000000	0.800000000	0.700000000

Source: JRC, 2024

The scattering phase function (normalized to 4π) can be modelled either through its Legendre coefficients x_k (see Eq. 9) ingested by the code through an ad-hoc file (see Fig. 11), or alternatively parameterized as a Two-Term Henyey-Greenstein (TTHG) phase function. The latter is the weighted sum of two single term Henyey-Greenstein (HG) phase functions (Henyey and Greenstein, 1941)

$$p_{HG}(\eta; g) = as \cdot \frac{1-g^2}{(1-2g\eta+g^2)^{\frac{3}{2}}} \quad (18)$$

in the form

$$p_{TTHG}(\eta; g_1, g_2, as) = as \cdot p_{HG}(g_1) + (1 - as) \cdot p_{HG}(-g_2) , \quad (17)$$

and parameters g_1 , g_2 and as (all ranging between 0 and 1) must be provided.

The ocean bottom can be modelled either as a Lambertian reflecting surface of given albedo A , or as a surface characterized by a HG bi-directional reflectance function of parameter g . Parameters A and g must be provided.

In the absence of water layers the FEM code solves the RTE for an atmosphere bounded by a land surface.

The number N of grid points for the half-interval of the angular variable (see eq. 15), must be also defined: this parameter sets the accuracy of the computation (see Section 3.3).

Figure 11. Example of input file containing the Legendre moments of the phase function (e.g., *momname.dat*).

```

1 3
1 1.000000000000
2 0.000000000000
3 0.500000000000
2 3
1 1.000000000000
2 0.000000000000
3 0.500000000000
3 3
1 1.000000000000
2 0.000000000000
3 0.500000000000
4 3
1 1.000000000000
2 0.000000000000
3 0.500000000000

```

Source: JRC, 2024

Definition of the output characteristics

The FEM code is able to compute the irradiance and the angular distribution of the diffuse radiance at any optical thickness.

The definition of the output characteristics must specify *i*) which products have to be computed (radiance and/or irradiance), *ii*) the output optical thicknesses (computed from the TOA), and *iii*) the output radiance propagation directions. The latter is defined by the azimuth angle ϕ measured with respect to the azimuth of the solar beam, and the cosine η of its polar angle θ measured from the τ axis: positive cosines correspond to downgoing radiance, negative cosines to upgoing one. Fig. 12 displays an example of input file defining the output characteristics (e.g., *card2.dat*); Fig. 13 illustrates the applied reference geometry.

Figure 12. Example of input file defining the output characteristics (e.g., *card2.dat*)

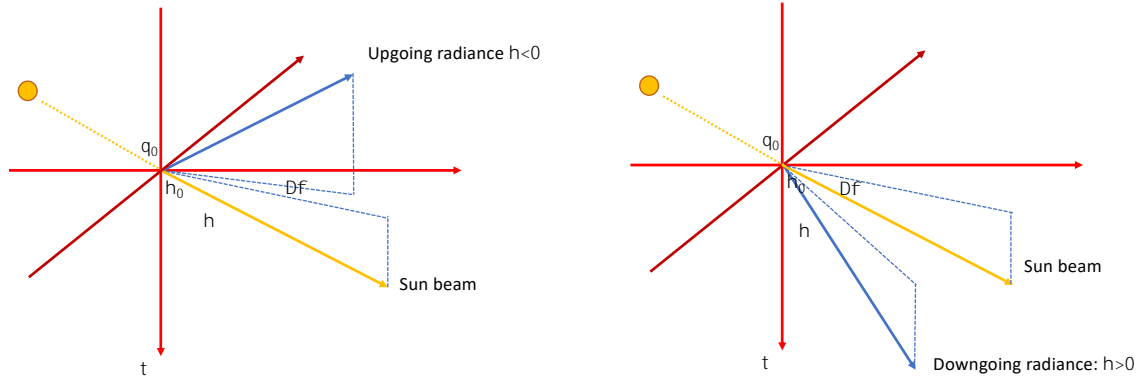
```

=====
                        OUTPUT CHARACTERISTICS
=====
Radiance:                1
Irradiance:              1
=====
Harmonic number          -1
# Computational Optical Depth (incr.ord.): 4
                                0.00000000
                                0.59999999
                                0.60000001
                                16.60000000
# Computational azimuth angles (deg) (incr.ord.) 1
                                0.d0
# Computational polar angles (incr.ord.) 10
equidistributed between [-1,1] 1
                                -1.00
                                -0.90
                                -0.80
                                -0.70
                                -0.60
                                -0.50
                                -0.40
                                -0.30
                                -0.20
                                -0.10

```

Source: JRC, 2024

Figure 13. the Applied reference geometry: $\eta_0 = \cos \theta_0$; $\eta = \cos \theta$; $\Delta\phi$ is the radiance azimuth with respect to the sun-beam azimuth. Zenith angles are computed with respect to the τ axis.



Source: JRC, 2024

Examples of the output files are given in Fig. 14 to 15; the detailed description of their format is given in Appendix A.3.

Figure 14. Example of uncommented output file (e.g., *ofname.dat*)

0.0000000000000000	
-1.0000000000000000	3.05791759748390707E-002
-0.9000000000000000	2.6995715837792664E-002
-0.8000000000000000	2.9305389918043284E-002
-0.6999999999999999	3.30227379016303274E-002
-0.5999999999999999	3.78934747304284686E-002
-0.5000000000000000	4.41038113604450208E-002
-0.3999999999999999	5.20155736190499084E-002
-0.2999999999999999	7.18130689578463566E-002
-0.1999999999999999	7.30589214287796079E-002
-9.99999999999999778E-002	8.51334465568725079E-002
0.1000000000000001	0.0000000000000000
0.2000000000000001	0.0000000000000000
0.3000000000000001	0.0000000000000000
0.4000000000000002	0.0000000000000000
0.5000000000000000	0.0000000000000000
0.6000000000000009	0.0000000000000000
0.7000000000000007	0.0000000000000000
0.8000000000000004	0.0000000000000000
0.9000000000000002	0.0000000000000000
1.0000000000000000	0.0000000000000000
0.5999999999999999	
-1.0000000000000000	8.74912946034791736E-003
-0.9000000000000000	7.61503125431677984E-003
-0.8000000000000004	6.29521115712039040E-003
-0.6999999999999999	9.58670353838999562E-003
-0.5999999999999999	1.5564886124060571E-002
-0.5000000000000000	1.45401492845849741E-002
-0.3999999999999999	1.92855667414978518E-002
-0.2999999999999999	2.71491116729718866E-002
-0.1999999999999999	4.02668145575730482E-002
-9.99999999999999778E-002	6.07175620203136701E-002
0.1000000000000001	0.060288511807027E-001
0.2000000000000001	0.116039457438516E-001
0.3000000000000004	0.125643361838153E-001
0.4000000000000002	0.132589620625976E-001
0.5000000000000000	0.1371353953647723E-001
0.6000000000000009	0.1345560677942822E-001
0.7000000000000007	0.1195595895749392E-001
0.8000000000000004	9.27524312316809207E-002
0.9000000000000002	9.19713721506626319E-002
1.0000000000000000	2.88084356251148560E-002
0.6000000000000009	
-1.0000000000000000	1.49514171821675656E-002
-0.9000000000000000	1.1183562345133400E-002
-0.8000000000000004	1.14936348058061345E-002
-0.6999999999999999	1.24026068154268129E-002
-0.5999999999999999	1.3653497392381756E-002
-0.5000000000000000	1.51805089342950209E-002
-0.3999999999999999	1.70027828388052544E-002
-0.2999999999999999	1.92247781942016562E-002
-0.1999999999999999	2.18104729120172786E-002
-9.99999999999999778E-002	2.45031166576589639E-002
0.1000000000000001	2.45031166831972513E-002
0.2000000000000001	2.18104729402008278E-002
0.3000000000000004	1.92247782371695181E-002
0.4000000000000002	1.70027829165987597E-002
0.5000000000000000	1.51805096090160099E-002
0.6000000000000009	1.36534976439532246E-002
0.7000000000000007	0.1856370541092595E-001
0.8000000000000004	0.2332786552604455E-001
0.9000000000000002	0.1570145529102711E-001
1.0000000000000000	5.10236864532088372E-002
16.6000000000000001	
-1.0000000000000000	4.37693063912269383E-006
-0.9000000000000000	4.37693063912269383E-006
-0.8000000000000004	4.37693063912269383E-006
-0.6999999999999999	4.37693063912269383E-006
-0.5999999999999999	4.37693063912269383E-006
-0.5000000000000000	4.37693063912269383E-006
-0.3999999999999999	4.37693063912269383E-006
-0.2999999999999999	4.37693063912269383E-006
-0.1999999999999999	4.37693063912269383E-006
-9.99999999999999778E-002	4.37693063912269383E-006
0.1000000000000001	3.37766343515841877E-006
0.2000000000000001	3.54845133681936172E-

Source: JRC, 2024

Figure 15. Example of verbose output file (e.g., ofname.out)

```

Spectral irradiance =      1.0000000000000000
Solar zenith angle (deg) =    50.0000000000000000
Surface albedo =          0.5000000000000000
Surface asymmetry factor =    0.0000000000000000
Number of grid points for half interval =      4

Refractive Index
Atmospheric Layers      2      1.00000
Water Layers            2      1.34100

Layers characteristics:
nl      ssa      Tau-tot
1      0.750000000    0.400000000
2      0.000000000    0.600000000
3      0.850000000    9.100000000
4      0.600000000    16.600000000

Henyey-Greenstein =      true

nl      g1      g2      as
1      0.500000000    0.400000000    0.500000000
2      0.600000000    0.500000000    0.800000000
3      0.900000000    0.700000000    0.950000000
4      0.200000000    0.800000000    0.700000000

RADIANCE
tau = 0.0000000000000000
azimuth = 0.0000000000000000
Cos(polar angle)      Radiance Value
-1.0000000000000000    3.05791759748390707E-002
-0.9000000000000000    2.69957515837792664E-002
-0.8000000000000000    2.93053099180432849E-002
-0.6999999999999999    3.30227379016303224E-002
-0.5999999999999999    3.78934747430246868E-002
-0.5000000000000000    4.41038113604450200E-002
-0.3999999999999999    5.20155736190499804E-002
-0.2999999999999999    6.18130609578463566E-002
-0.1999999999999999    7.30589214287796079E-002
-0.9999999999999999    8.51334465568775079E-002
0.1000000000000000    0.0000000000000000
0.2000000000000000    0.0000000000000000
0.3000000000000000    0.0000000000000000
0.4000000000000000    0.0000000000000000
0.5000000000000000    0.0000000000000000
0.6000000000000000    0.0000000000000000
0.7000000000000000    0.0000000000000000
0.8000000000000000    0.0000000000000000
0.9000000000000000    0.0000000000000000
1.0000000000000000    0.0000000000000000
tau = 0.5999999999999999
azimuth = 0.0000000000000000
Cos(polar angle)      Radiance Value
-1.0000000000000000    8.74912946034791736E-003
-0.9000000000000000    7.61503125431677904E-003
-0.8000000000000000    8.29512115712039040E-003
-0.6999999999999999    9.58670358388999562E-003
-0.5999999999999999    1.15548861240605781E-002
-0.5000000000000000    1.45401492845846914E-002
-0.3999999999999999    1.92055667414970518E-002
-0.2999999999999999    2.71491116729718866E-002
-0.1999999999999999    4.02668145575730482E-002
-0.9999999999999999    6.07175620203136701E-002
0.1000000000000000    0.10602085110070227
0.2000000000000000    0.11760394574385163
0.3000000000000000    0.12564336183381530
0.4000000000000000    0.13258596206259768
0.5000000000000000    0.13713539536477234
0.6000000000000000    0.13455606779428222
0.7000000000000000    0.11955958957943928
0.8000000000000000    9.27524312316809207E-002
0.9000000000000000    6.19713721506626319E-002
1.0000000000000000    2.88084356251148560E-002
tau = 0.6000000000000000
azimuth = 0.0000000000000000
Cos(polar angle)      Radiance Value
-1.0000000000000000    1.49514171821675656E-002
-0.9000000000000000    1.11835562345133400E-002

```

Source: JRC, 2024

cont.


```

-0.8000000000000004      1.14936348058061345E-002
-0.6999999999999996      1.24026068154268129E-002
-0.5999999999999998      1.36534973929381756E-002
-0.5000000000000000      1.51805089342950290E-002
-0.3999999999999991      1.70027828388052554E-002
-0.2999999999999993      1.92247781942016562E-002
-0.1999999999999996      2.18104729120172786E-002
-9.9999999999999778E-002  2.45031166576589639E-002
0.10000000000000001      2.45031166831975213E-002
0.20000000000000001      2.18104729402008278E-002
0.30000000000000004      1.92247782371695101E-002
0.40000000000000002      1.70027829165907597E-002
0.50000000000000000      1.51805090690160099E-002
0.60000000000000009      1.36534976439532246E-002
0.70000000000000007      0.18563705410925951
0.80000000000000004      0.23327865526044553
0.90000000000000002      0.15701455291027119
1.0000000000000000      5.10236864532088372E-002
tau = 16.600000000000001
azimuth = 0.000000000000000
Cos(polar angle)      Radiance Value
-1.0000000000000000      4.37693063912269383E-006
-0.90000000000000002      4.37693063912269383E-006
-0.80000000000000004      4.37693063912269383E-006
-0.6999999999999996      4.37693063912269383E-006
-0.5999999999999998      4.37693063912269383E-006
-0.50000000000000000      4.37693063912269383E-006
-0.3999999999999991      4.37693063912269383E-006
-0.2999999999999993      4.37693063912269383E-006
-0.1999999999999996      4.37693063912269383E-006
-9.9999999999999778E-002  4.37693063912269383E-006
0.10000000000000001      3.37766343515841877E-006
0.20000000000000001      3.54845133681936172E-006
0.30000000000000004      3.80529024085902860E-006
0.40000000000000002      4.17066355488659645E-006
0.50000000000000000      4.69393011700548703E-006
0.60000000000000009      5.48952992310058312E-006
0.70000000000000007      6.90654002905930826E-006
0.80000000000000004      1.00578597761362356E-005
0.90000000000000002      1.62983053185555353E-005
1.0000000000000000      2.26233121473524911E-005

IRRADIANCE
tau = 0.000000000000000
Upgoing diffuse irradiance = -0.13578827399573168
Downgoing diffuse irradiance = 0.000000000000000
Downgoing direct irradiance = 0.64278760968653947
Reflected direct irradiance = -3.45699020199739383E-003
TOTAL IRRADIANCE = 0.50354233748801039
tau = 0.59999999999999981
Upgoing diffuse irradiance = -3.65118866130168529E-002
Downgoing diffuse irradiance = 0.14161364192454956
Downgoing direct irradiance = 0.25274474429081012
Reflected direct irradiance = -0.79193597947099462E-003
TOTAL IRRADIANCE = 0.34905456362287185
tau = 0.60000000000000005
Upgoing diffuse irradiance = -4.98890492882839709E-002
Downgoing diffuse irradiance = 0.15490650935417413
Transmitted direct irradiance = 0.24395200760723840
TOTAL IRRADIANCE = 0.34905026767312863
tau = 16.600000000000001
Upgoing diffuse irradiance = -1.37505331411399075E-005
Downgoing diffuse irradiance = 2.75002320445984926E-005
Transmitted direct irradiance = 8.34237681369255240E-010
TOTAL IRRADIANCE = 1.37505331411399550E-005

```

Source: JRC, 2024

In the presence of a smooth air-water interface, the upgoing radiance in the atmosphere and the downgoing refracted radiance in the water include a singular component corresponding to the reflected or refracted solar beam, respectively. Notably, the printed output radiance values refer to the sole diffuse radiance.

Since the reflected radiance flux is a finite value, irradiance outputs include both diffuse and reflected or refracted direct irradiances, which are separately presented.

It is specified that: the term *diffuse* indicates the radiance which underwent at least one scattering event within the medium; the term *direct* defines the radiance which interacted neither with the media, nor with the air-water interface or with the surface; the term *reflected* designates the radiance which interacted with the surface or with the air-water interface; and the term *refracted* refers to the radiance that crossed the air-water interface.

It is clear that the reflected radiance propagates upwards, while direct and refracted radiances propagate downwards.

3.3 FEM code accuracy

The accuracy of the radiance solution is controlled by two parameters: ϵ , which defines the threshold value for L^m in the radiance Fourier series (if $L^m \leq \epsilon$ the series of Eq. 13 is truncated), and the number of grid points N (see Eq. 15), which defines the accuracy in the computation of each radiance harmonics L^m . The parameter ϵ is a hard-coded variable, whose default value is set to 10^{-4} . The number of grid points N must be defined by the user.

Although these two parameters are formally independent, the optimal balance between accuracy and CPU time consumption is obtained when ϵ and the accuracy in the computation of L^m are of the same order of magnitude. The number of grid points N necessary to obtain the desired overall accuracy strictly depends on the gradient of the angular radiance distribution, and hence on phase functions and output geometry. In typical radiance computations at TOA, where the radiance angular distribution is rather smooth, an overall accuracy of 10^{-4} is reached with 6-8 grid points. For highly peaked phase functions, especially if radiances below the air-water interface are required, 16 or even more grid points are needed for the desired accuracy. The simulation of the downgoing radiance around the direction of the sunbeam in the atmosphere or around the direction of the refracted sunbeam in the water, might require up to 64 grid points.

Notably, the accuracy of irradiance computations only depends on the number of grid points N , and it is generally higher than the radiance accuracy for any given number of grid points. For example, $N=2$ is mostly sufficient to achieve an accuracy of 10^{-3} ; $N=4$ is recommended to reach accuracies of about 10^{-4} .

Specific tests on flux conservation for a totally conservative medium characterized by extremely forward peaked phase functions were performed in (Bulgarelli et al., 1999). For both typical air-water refractive index ($n=1.341$) and for a more extreme case ($n=2$) the accuracy in flux conservation was shown to be at least 10^{-3} even for the lowest number of grid points $N=2$.

A comprehensive assessment on radiance computational accuracy was conducted in (Bulgarelli et al., 1999) for realistic test cases coupling several Low-Resolution Transmission Model (LOWTRAN) atmospheres (Kneizys et al., 1988), i.e.:

1. urban aerosol with 5 km visibility;
2. rural aerosol with 23 km visibility;
3. maritime aerosol with 80% relative humidity;
4. advective fog with 0.2 km in visibility;
5. stratocumulus clouds between 0.66 and 2.0 Km,

with typical coastal optical stratifications:

- a) two-layers profile with a moderate difference in optical properties;
- b) two-layers profile with a highly scattering surface layer;
- c) four-layers profile with a highly scattering intermediate layer.

Mean and maximum Relative Error (RE) over 209 viewing angles at TOA for FEM computations obtained with sole $N=4$ grid points with respect to the fully converged solution ($N=64$) are summarized in Table 1. Overall results showed a mean difference of 0.2%, and a maximum relative difference never exceeding 0.6%.

Table 1. mean and absolute Relative Error (RE) between FEM($N=4$) and FEM($N=64$) values computed at TOA over 209 viewing angles with $\theta_0=45^\circ$ for sample test cases

Test case	1a	2a	3a	3b	3c	4a	5a
Mean $ RE \times 10^{-3}$	0.7	1.1	1.6	1.5	1.1	0.9	0.5
Max RE $\times 10^{-3}$	1.7	5.5	4.4	4.3	4.0	5.8	0.9

Source: Bulgarelli et al., 1999

4 FEM code validation

The FEM code has been extensively validated through benchmark with data from literature, other codes and *in situ* data. The following Section summarizes main results from validations, while for details, the reader is referred to the original works.

4.1 Benchmark with data from the literature

Several numerical models for the simulation of the in-water light field were intercompared by Mobley et al. (1993) over a set of canonical problems drawn from optical oceanography. The stratified water problem was used to test the correctness of FEM implementation (Bulgarelli et al., 1999). This implied the simulation at discrete water depths of the downward irradiance E_d ,

$$E_d \equiv \int_{\Omega_d} L_\lambda \cos\theta d\Omega, \quad (18)$$

(where Ω_d encompasses all downward directions); the upward scalar irradiance E_{ou}

$$E_{ou} \equiv \int_{\Omega_u} L_\lambda d\Omega, \quad (19)$$

(where Ω_u encompasses all upward directions) and the upwelling nadir radiance L_u (i.e., the radiance measured by a sensor pointing in the nadir direction). Table 2 summarizes values provided by (Mobley et al., 1993) and values simulated with FEM(N=4) and FEM(N=64), showing that optimal agreement is already reached with FEM(N=4).

Table 2. Average Values of E_d , E_{ou} , and L_u at selected depths from Mobley et al., (1993), Problem 3, with sample standard deviations, and corresponding values obtained with FEM(N=4) and FEM(N= 64)

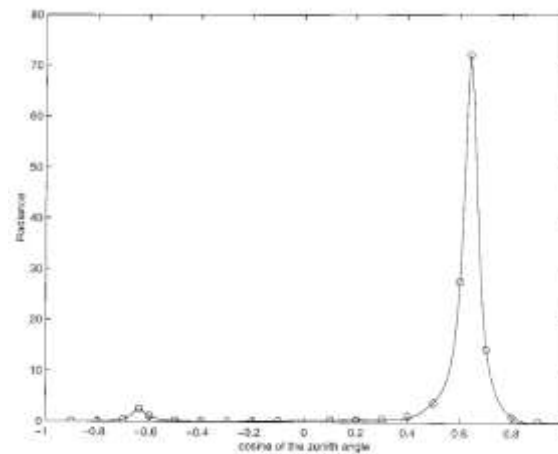
Depth (m)	Mobley et al. Average Values		
	$E_d \pm \sigma$	$E_{ou} \pm \sigma$	$L_u \pm \sigma$
5	$2.30 \times 10^{-3} \pm 1.38 \times 10^{-3}$	$4.34 \times 10^{-2} \pm 1.08 \times 10^{-3}$	$3.13 \times 10^{-2} \pm 1.69 \times 10^{-4}$
25	$1.62 \times 10^{-3} \pm 4.54 \times 10^{-5}$	$2.86 \times 10^{-4} \pm 1.09 \times 10^{-5}$	$2.12 \times 10^{-5} \pm 1.29 \times 10^{-6}$
60	$5.23 \times 10^{-5} \pm 3.71 \times 10^{-6}$	$5.13 \times 10^{-6} \pm 1.85 \times 10^{-7}$	$3.57 \times 10^{-7} \pm 1.55 \times 10^{-7}$
	FEM (N = 4) values		
	E_d	E_{ou}	L_u
5	2.31×10^{-3}	4.37×10^{-2}	3.15×10^{-3}
25	1.62×10^{-3}	2.90×10^{-4}	2.09×10^{-5}
60	5.22×10^{-5}	5.42×10^{-6}	4.43×10^{-7}
	FEM (N = 64) values		
	E_d	E_{ou}	L_u
5	2.31×10^{-3}	4.36×10^{-2}	3.15×10^{-3}
25	1.61×10^{-3}	2.88×10^{-4}	2.09×10^{-5}
60	5.21×10^{-5}	5.40×10^{-6}	4.43×10^{-7}

Source: Bulgarelli et al., 1999

4.2 Benchmark with the MC code by Roberti (1997)

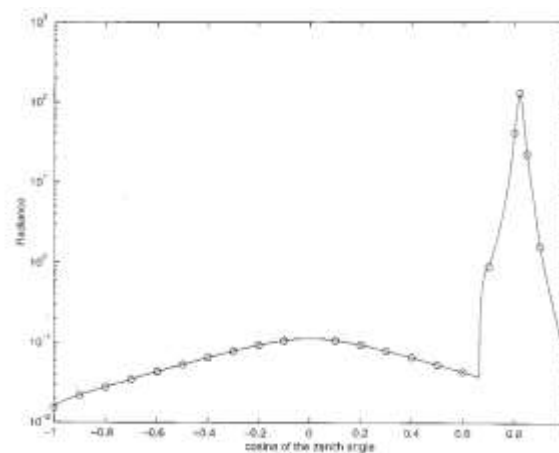
The ability of FEM to compute the angular distribution of the radiance in the presence of highly forward peaked phase functions was assessed (Bulgarelli et al., 1999) through comparison with values obtained with the backward Monte Carlo code developed by (Roberti, 1997) (MC-R). The intercomparison was performed for an idealized two-layer atmosphere-ocean system characterized by highly asymmetric phase function (HG $g=0.95$) and high single-scattering albedo ($\omega_0=0.9$). An excellent agreement between FEM and MC-R results was shown at all selected optical depths and for the entire angular range, even in correspondence of extremely pronounced radiance angular variations. Example of radiance angular distributions just above and just below the water surface are displayed in Fig. 16 and 17, respectively. Results are provided in the solar plane with $\theta_0=50^\circ$ and assuming $E_0=n \text{ Wm}^{-2} \text{ nm}^{-1}$. Incidentally, the atmospheric downgoing diffuse radiance peaks around the sun beam direction ($n=0.64$), while a smaller peak in the upgoing diffuse radiance appears in correspondence of the direction of the reflected sun beam ($n=-0.64$) (Fig. 16). Also, the in-water downgoing radiance peaks around the refracted sun beam ($n=0.82$), while the sharp drop at $n=0.67$ corresponds to the cosine of the critical angle beyond which total internal reflection arises (Fig. 17).

Figure 16. Radiance [$\text{Wm}^{-2} \text{nm}^{-1} \text{sr}^{-1}$] simulated with FEM($N=64$) just above the air–water interface. Empty circles indicate results obtained with MC-R (Roberti, 1997) initializing 10^6 photons.



Source: Bulgarelli et al., 1999

Figure 17. Radiance [$\text{Wm}^{-2}\text{nm}^{-1}\text{sr}^{-1}$] simulated with FEM($N=64$) just below the air–water interface. Empty circles indicate results obtained with MC-R (Roberti, 1997) with 10^6 photons.



Source: Bulgarelli et al., 1999

4.3 Benchmark with the PHO-TRAN code

In the frame of an extensive and comprehensive exercise to assess the accuracy of radiative transfer models in the simulation of the full radiance distribution within the atmosphere-ocean system (Bulgarelli and Doyle, 2004), the FEM and the PHO-TRAN 3D backward MC code (Doyle and Rief, 1998) were intercompared at different optical depths for a set of idealized test cases:

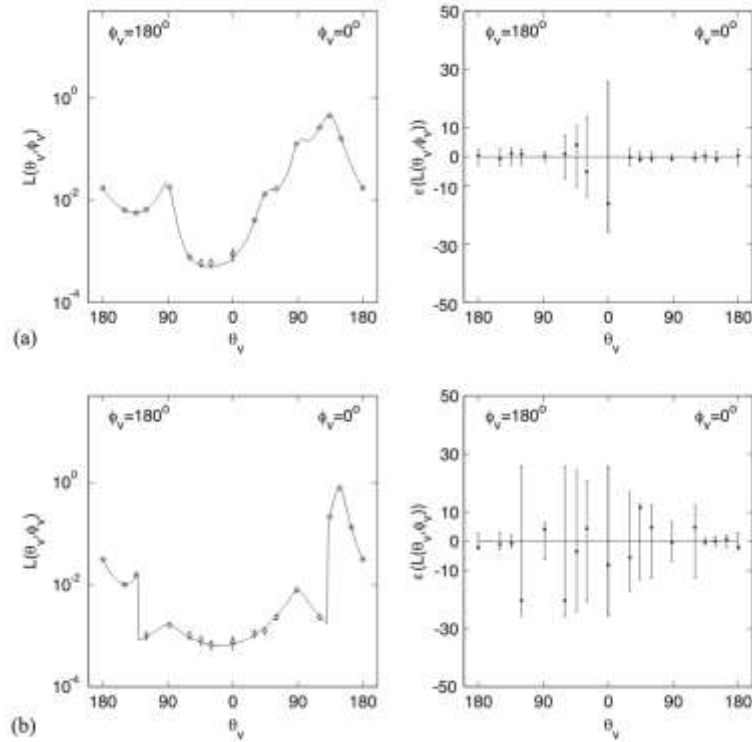
1. Standard problem: two-layer system with a moderate forward peaked atmospheric phase function and a highly scattering and infinitely deep water;
2. The standard problem but with a highly forward scattering atmosphere;
3. The standard problem but with a highly absorbing water;
4. The standard problem including a bottom floor with Lambertian reflectivity;
5. Problem 4 for a shallow water.

A realistic case, designed from experimental data (Zibordi et al., 2002), was additionally outlined to compare in-water profiles of L_u , E_d and upwelling irradiance E_u (where the mathematical definition of E_u is obtained from Eq. 18 integrating over all upward directions Ω_u).

Optimal agreement was shown between the two codes under any condition, with relative differences always lower than the estimated statistical error of PHO-TRAN data (Bulgarelli and Doyle, 2004).

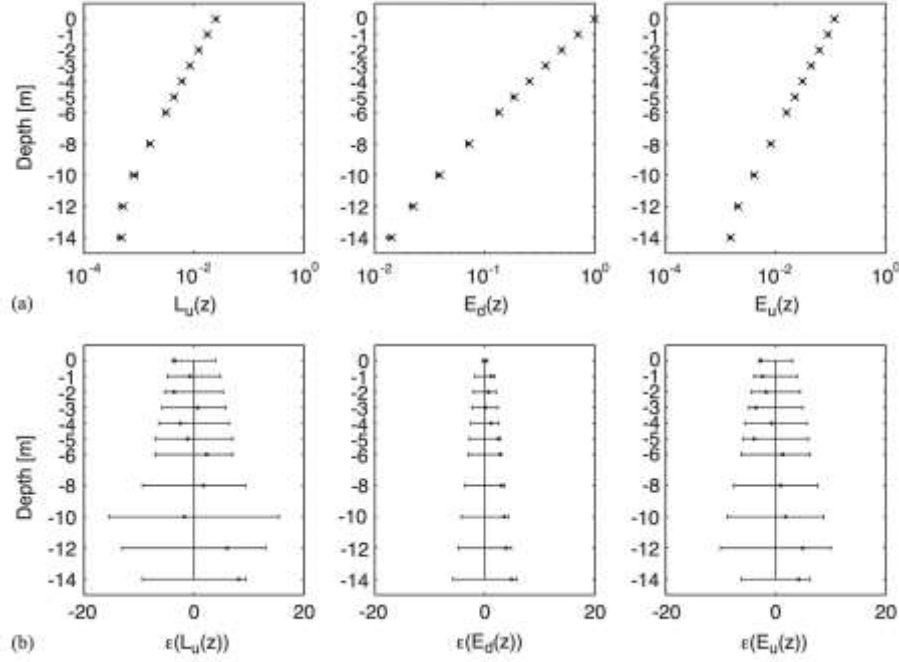
Sample results are illustrated in Fig. 18 and 19.

Figure 18. Intercomparison between (-) FEM(N=64) and (•) PHO-TRAN(10^5 photons) simulated values for problem 3 ($\theta_0=45^\circ$, $\Phi_0=0^\circ$, $E_0=1 \text{ W m}^{-2}\text{nm}^{-1}\text{sr}^{-1}$). The radiance angular distributions [$\text{Wm}^{-2}\text{nm}^{-1}\text{sr}^{-1}$] is displayed on the left panels, while the relative percentage differences, with bars representing the 99% confidence on the PHO-TRAN results, are shown on the right panels. The upper panels (a) display results just above the water surface, while the lower panels (b) show results just beneath the water surface. The symbols θ_v and Φ_v indicate the viewing direction with $\theta=180^\circ-\theta_v$ and $\Phi=180^\circ+\Phi_v$. $0^\circ<\theta_v<90^\circ$ indicates down-looking directions while $90^\circ<\theta_v<180^\circ$ refers to the up-looking directions.



Source: Bulgarelli and Doyle, 2004

Figure 19. Intercomparison between (x) FEM(N=64) and (•) PHO-TRAN(10^5 photons) simulations for the realistic problem. Panels (a) display in-water profiles of nadir L_u [$\text{W m}^{-2}\text{nm}^{-1}\text{sr}^{-1}$], E_d and E_u [$\text{Wm}^{-2}\text{nm}^{-1}$] while panels (b) illustrate the correspondent relative differences. Bars represent the 99% confidence on PHO-TRAN results.

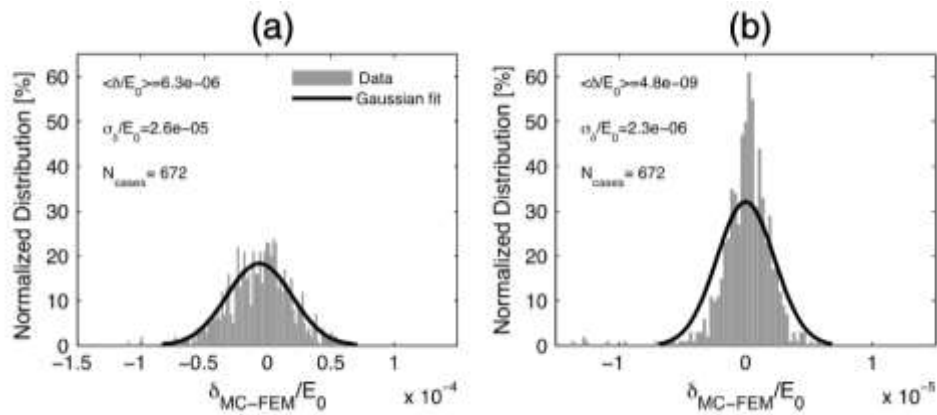


Source: Bulgarelli and Doyle, 2004

4.4 Benchmark with the NAUSICAA code

Excellent agreement was additionally found between TOA radiances simulated with FEM and with the NAUSICAA backward 3D MC code (Bulgarelli et al., 2014) over *a)* a uniform ideal (lossless) and perfectly isotropic (Lambertian) surface and *b)* a Fresnel-reflecting surface, for a set of atmospheric test-cases typically encountered in coastal regions (Bulgarelli et al., 2014). Results are summarized in Fig. 20.

Figure 20. Normalized distributions of $\delta_{\text{MC-FEM}}/E_0 = (L_{\text{MC}} - L_{\text{FEM}})/E_0$ [sr^{-1}] over 672 test cases between TOA radiances computed with FEM(N=64) and NAUSICAA (10^7 photons) assuming (a) a uniform ideal Lambertian surface and (b) a uniform Fresnel-reflecting surface. The Gaussian fit of the distributions is displayed in black. Its mean $\langle \delta/E_0 \rangle$ and standard deviation σ_δ/E_0 are also given. Note that the scale for the Lambertian case is one order of magnitude higher than that of the Fresnel case.



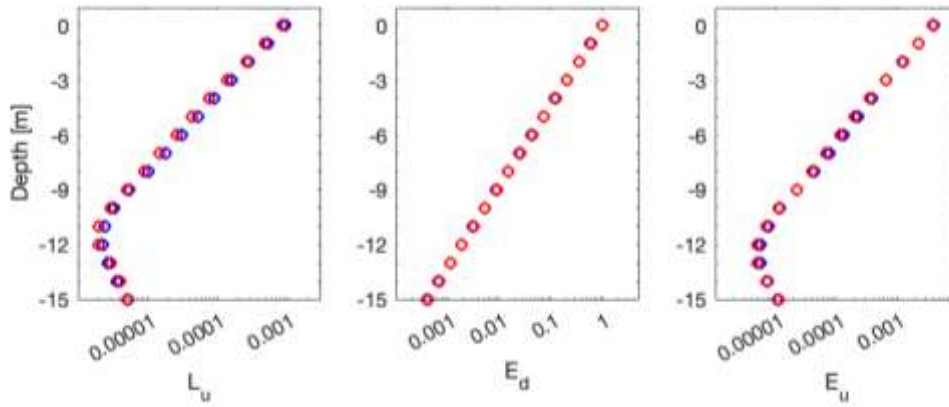
Source: Bulgarelli et al., 2014

Notably, since the FEM and MC schemes rely on fundamentally different approaches to solve the RTE, the outstanding agreement between FEM and MC-R, PHO-TRAN and NAUSICAA represents a solid validation of the physical implementations in each code.

4.5 Benchmark with Hydrolight

The intercomparison with the popular Hydrolight 4.1 code (Mobley et al., 1993) was performed (Bulgarelli et al., 2003b) with a realistic case designed from experimental data (Zibordi et al., 2002) for a slightly stratified water volume. Results reported in Fig. 21 shows optimal agreement of L_u , E_u and E_d in-water profiles.

Figure 21. In-water profiles of L_u , E_u and E_d at 665 nm (normalized to the subsurface downward irradiance) simulated with (red circles) FEM and with (blue circles) Hydrolight 4.1.

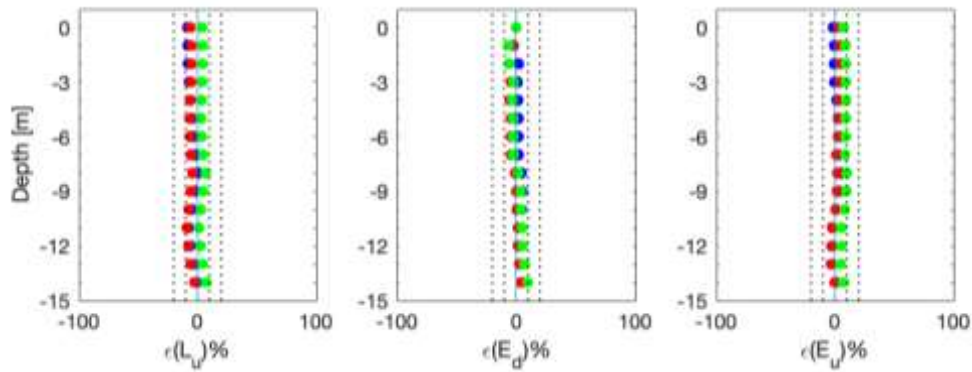


Source: Bulgarelli et al., 2003b

4.6 Benchmark with experimental *in situ* data

Within the frame of a closure experiment, FEM demonstrated its ability to reproduce *in situ* measurements of above- and in-water apparent optical properties (AOPs) when ingesting corresponding measurements of the inherent optical properties (IOPs). Differences between modelled and measured AOPs were within the uncertainties estimated for the *in situ* measurements (Bulgarelli et al., 2003b). Sample results are presented in Fig. 22.

Figure 22. In-water profiles of relative differences $\epsilon(L_u)$, $\epsilon(E_u)$, and $\epsilon(E_d)$ at (blue) 412, (red) 490, and (green) 555 nm between experimental and FEM theoretical data: $\epsilon(x) = 100 \cdot (x_{FEM}/x_{exp} - 1)$. The dotted lines delimit the $\pm 10\%$ and $\pm 20\%$ regions.



Source: Bulgarelli et al., 2003b

5 FEM code applications

The FEM numerical code has been extensively applied over the years to support the processing and the validation of satellite data, and for the analysis of uncertainties affecting *in situ* and satellite data.

5.1 Simulation of the signal at satellite sensors in support to the processing and accuracy assessment of satellite data

Back in 2003 FEM was applied in a pioneer study to assess the accuracy of an in-house approximate atmospheric correction code (Bulgarelli and Melin, 2000) for the processing of Sea Wide Field Viewing Sensor (SeaWiFS) data (Bulgarelli and Zibordi, 2003) (Bulgarelli et al., 2003a). The FEM code was employed to investigate a set of typical and extreme measurement conditions encountered in European marine regions by simulating the radiance received by the satellite sensor, together with its separate components (e.g., aerosol radiance, Rayleigh radiance, water leaving radiance,...). The analysis showed that the coupling of an approximate atmospheric correction method with the vicarious calibration of the space sensor is a valuable solution for the estimate of atmospheric and water parameters. Over different simulated measurement conditions, the study theoretically estimated the uncertainties in the determination of the aerosol optical thickness at 865 nm, the aerosol Ångström exponent, the water leaving radiance and the ratio between the remote sensing reflectance R_{rs} at 490 and 555 nm. Remarkably, results were confirmed by the analysis of 59 match-ups between satellite-derived and *in situ* measurements for a site located in the central Baltic.

FEM simulations of the radiometric signal at TOA and at the surface were also employed for the analysis of aerosol direct radiative effects and forcing efficiency in the Adriatic Sea within an investigation on aerosol variability in the region benefitting from SeaWiFS and autonomous ground measurements (Mélin et al., 2006).

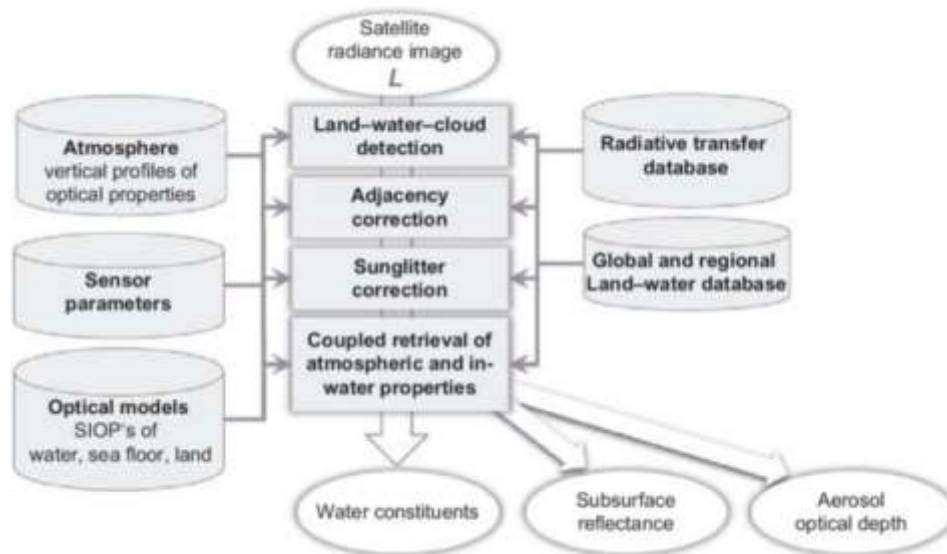
Within the frame of comprehensive investigations on adjacency effects in OC data from coastal waters (Bulgarelli et al., 2018, 2014; Bulgarelli and Zibordi, 2018a, 2018b), the FEM code was extensively applied to simulate the atmospheric radiance received by satellite sensors for a wide range of representative illumination and atmospheric conditions typical of mid-latitude coastal regions. The investigation was specifically targeted to the evaluation of nearby-land perturbations in Copernicus Sentinel-3 data acquired from coastal waters by the Ocean and Land Colour Instrument (OLCI) sensor. Specific investigations were also executed for the analysis of adjacency effects at a candidate European site for system vicarious calibration (SVC) of OLCI data (Bulgarelli and Zibordi, 2020).

The FEM code has been employed to build the radiative transfer database of precomputed TOA and surface radiances included in the Modular Inversion and Processing System (MIP) (Heege et al., 2014) (Kiselev et al., 2015), which is a model-inversion algorithm for the processing of satellite marine and inland water data initiated by the German Aerospace Center (Riha and Krawczyk, 2013) and further developed by EOMAP. MIP scheme is displayed in Fig. 23.

MIP is routinely employed to process imagery from different satellite missions for the monitoring of the aquatic environment (Bresciani et al., 2019; Dörnhöfer et al., 2017; Hartmann et al., 2021; Heege et al., 2014). Notably, it serves as data processor for the UNESCO World Water Quality Portal, conceptualized and developed in the framework of the International Initiative on Water Quality (IIWQ). It showcases and demonstrates the potential of remote sensing and satellite EO to improve water quality monitoring for a sustainable water resources management (IIWQ, 2018) (Heege et al., 2019).

Remarkably, MIP is the operational processor of water data within the Environmental Mapping and Analysis Program (EnMAP), a high-resolution imaging spectroscopy remote sensing mission successfully launched in 2022 (Storch et al., 2023).

Figure 23. Scheme of the MIP modules for water-quality processing



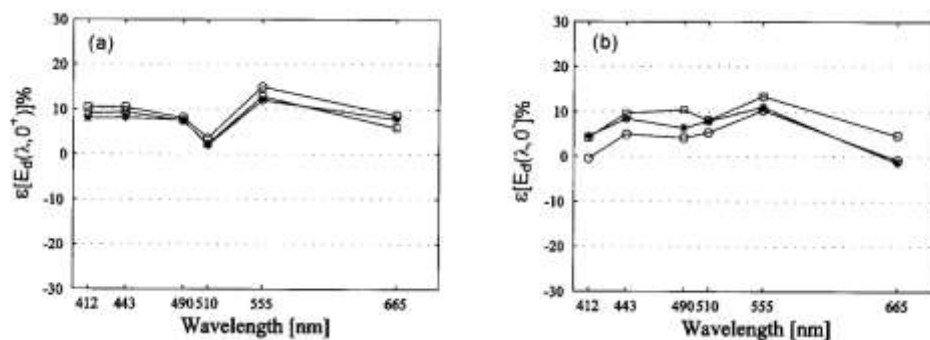
Source: Heege et al., 2014.

5.2 Simulation of the in-water light field in support to the development of bio-optical algorithms

Aiming at quantifying uncertainties affecting the modelling of coastal water radiometric quantities utilized for the validation of satellite OC data, an original closure experiment was performed in 2003 by intercomparing spectral underwater theoretical and experimental radiometric data (Bulgarelli et al., 2003b). Specifically, the study focused on above-water downward irradiance E_d and in-water spectral profiles of L_u , E_u , E_d , E_u/L_u (the nadir Q -factor) and E_u/E_d (the irradiance reflectance). Theoretical data were produced with the FEM code ingesting *in situ* atmospheric and marine inherent optical properties. The experimental data were taken from a comprehensive coastal-water data set collected in the northern Adriatic Sea (Zibordi et al., 2002). Under various measurement conditions, differences between theoretical and experimental data were quantified and analysed (see Fig. 22). These differences allowed showing a high sensitivity to experimental uncertainties in a few input quantities used for the simulations: the seawater absorption coefficient; the hydrosol phase function backscattering probability; and, mainly for clear water, the ocean bottom reflectance. Overall results restated the need for an accurate modelling of the propagation system (in particular, the water) for the simulation of in-water radiometric quantities. In specific, the analysis evidenced the need to select, on a layer-by-layer basis, a hydrosol phase function with appropriate backscattering probability and shape, proving that the arbitrary use of a single particulate phase function (e.g., the average Petzold phase function (Petzold, 1972, at that time routinely applied) could heavily affect the accuracy of the simulated results.

This same closure exercise highlighted a systematic spectral bias between theoretical and experimental in-air downward irradiances (Fig.24), suggesting a non-ideal cosine response of the irradiance collectors. FEM simulations were successively applied to support comprehensive investigations on cosine errors in irradiance measurements from field OC radiometers. Results suggested the implementation of a correction scheme to mitigate the impact of cosine errors when striving for high-accuracy irradiance measurements (Zibordi and Bulgarelli, 2007).

Figure 24. Relative difference between theoretical and experimental E_d data just above the water surface for representative experimental test-cases.



Source: Bulgarelli et al., 2003b.

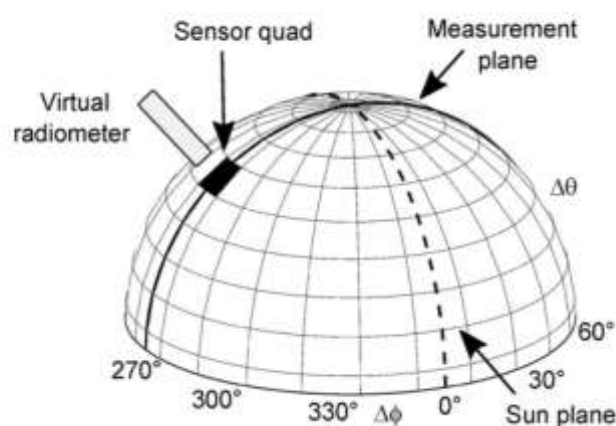
5.3 Simulation of the sky-radiance distribution in support to the assessment and minimization of uncertainties in *in situ* data

Theoretical simulations of the sky-radiance impinging on the water surface were utilized for a comprehensive investigation of sea-surface perturbations in above-water measurements.

The sky dome was divided into 684 quads (Fig. 25) and the radiance originating from the centroid of each quad was simulated at center-wavelengths relevant to OC applications, and for a wide and representative range of atmospheric and illumination conditions. Fig. 26 shows an example of sky-radiance distribution.

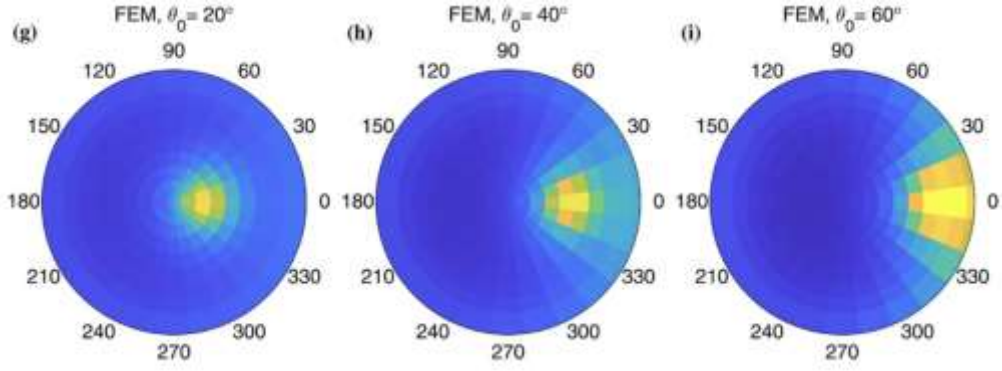
This database of simulated sky radiances allowed investigating spectral and atmospheric dependences of sea-surface perturbations in above-water measurements for the validation of OC satellite data (D'Alimonte et al., 2021) (Bulgarelli et al., 2022). Specific reference was given to measurement protocols and data quality control procedures applied within the Ocean Color component of the Aerosol Robotic Network (AERONET-OC) (Zibordi et al., 2010, 2009).

Figure 25. Partitioning of the upper hemisphere into quads. The thick solid and dashed lines indicate the measurement and the solar plane, respectively. The sensor-quad marked in black represents the virtual radiometer.



Source: D'Alimonte et al., 2021.

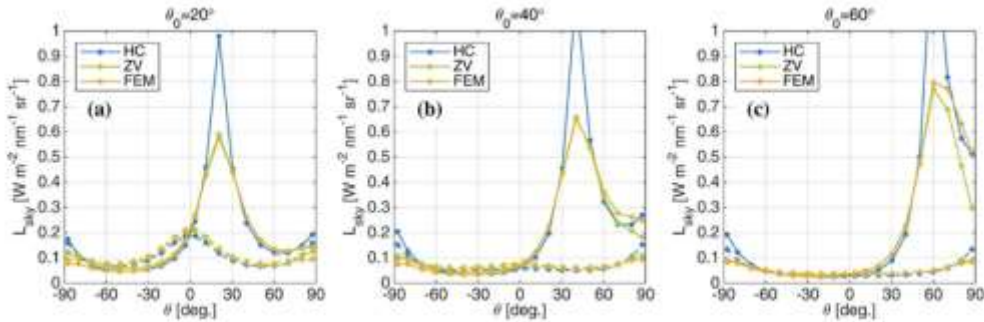
Figure 26. Example of diffuse sky-radiance distributions at 550 nm obtained with FEM(N=64) for $\theta_0 = 20^\circ$, 40° and 60°



Source: D'Alimonte et al., 2021

The rationale behind the adoption of the FEM code was substantiated by its capability to ensure highly accurate spectral and angular distributions of the diffuse atmospheric radiance, including an accurate determination of the sky radiance around the sunbeam direction (mostly affected by a correct treatment of the aerosol forward scattering) and near the horizon (mostly affected by a correct treatment of multiple scattering effects). Fig. 27 shows a comparison of the sky-radiance distribution in the solar and measurement planes computed with FEM, a simple analytic solution of the RTE (ZC) (Zibordi and Voss, 1989), and the Harrison and Coombs parameterization (HC) (Harrison and Coombes, 1988) implemented in Hydrolight (Mobley, 1994) (Mobley, 1999).

Figure 27. Diffuse sky radiance L_{sky} at 550 nm determined for the solar and measurement planes (solid and dashed lines, respectively) with HC, ZV and FEM for different θ_0 (i.e., 20° , 40° and 60°).



Source: D'Alimonte et al., 2021

FEM simulated sky radiances were additionally employed to support the analysis of *in situ* measurement methods for OC applications. Specifically, shading perturbations in the Sky-Blocked Approach (SBA) were investigated (Kajiyama et al., 2024).

Finally, in light of system vicarious calibration (SVC) activities undertaken by Copernicus and the European Organization for the Exploitation of Meteorological Satellites (EUMETSAT) for Sentinel-3/OLCI, FEM sky-radiance angular distributions for typical open-ocean atmospheric conditions were utilized to investigate shading effects in SVC optical buoys (Kajiyama et al., 2022).

6 Conclusions

The Copernicus Programme, established by the European Union in 2014 (Regulation EU No 377/2014), aims at creating a European capacity for Earth Observation by providing full, free, and open access to EO satellite and *in situ* data. This program plays a vital role in monitoring the implementation of the European Climate Law as part of the European Green Deal.

This Report is the first of a series dedicated to illustrate the long-standing experience of the JRC in developing and applying highly accurate radiative transfer models for the simulation of *in situ* and satellite data of the marine environment.

The in-house Advanced Radiative Transfer Models for In Situ and Satellite Ocean Color data (ARTEMIS-OC) software suite for the modelling of the signal received by *in situ* and satellite OC sensors comprises:

- The Finite Element Method radiative transfer code (FEM), to simulate the propagation of the solar radiation in a layered medium with diverse refractive indices (like the atmosphere-ocean system);
- The SkyFEM code for simulating the sky-radiance distribution;
- The FEMrad-OC code to comprehensively simulate the signal received by satellite OC sensors;
- The AquaFEM code for the simulation of radiance distribution and apparent optical properties within and just above any natural water body;
- The Novel Adjacency Perturbation Simulator for Coastal Areas (NAUSICAA), to compute adjacency perturbations induced by nearby land in OC data from coastal or inland water areas.

FEM is a highly accurate deterministic numerical model for the propagation of unpolarized solar radiation in an atmosphere-water system with horizontally invariant optical properties, as in open-ocean observations. NAUSICAA is a stochastic 3D MonteCarlo code for the propagation of the unpolarized solar radiation in an atmospheric medium bounded by an inhomogeneous reflecting surface, as it occurs in coastal or inland water regions.

SkyFEM, FEMrad-OC and AquaFEM are targeted configurations of the FEM code coupled with ad-hoc modelling of atmosphere and water.

Specific focus of the present report was to present the FEM code.

Benefitting of a short introduction on the basic principles of radiative transfer, the specific methodology implemented in FEM was thoroughly illustrated. A schematic description of the code followed, specifically detailing input requirements and formats, and layouts of provided outputs. Details on the accuracy of the FEM solution were additionally provided.

Evidence of the extensive validation of the FEM code was illustrated through a number of cases. FEM results were extensively validated over the years through comparison with data from the literature, benchmarks with other codes based on different mathematical techniques, and the performance of closure experiments with *in situ* data. The optimal agreement achieved ensures the correctness and reliability of FEM simulations, guarantying the fitness-for-purpose of the FEM code.

The FEM numerical code has served since decades in support to the creation of a European capacity for Earth Observations.

Evidence was presented of extensive applications of the FEM code in support of:

- the validation and calibration of satellite missions through the analysis of uncertainties affecting *in situ* and satellite data, with specific reference to the Copernicus S2 and S3 missions;
- bio-optical modelling, through the performance of closure experiments between modelled and measured in-water radiometric fields;
- the processing of satellite data for the monitoring of the aquatic environment exemplified by the Modular Inversion and Processing System (MIP) (Heege et al., 2014) (Kiselev et al., 2015), operationally applied to process water data within the high-resolution Environmental Mapping and Analysis Program (EnMAP) (Storch et al., 2023), which relies on a radiative transfer database built with FEM;

- the water quality monitoring for a sustainable water resources management (IIWQ, 2018). The same MIP serves as data processor for the UNESCO World Water Quality Portal, conceptualized and developed in the framework of the International Initiative on Water Quality (IIWQ) to showcase and demonstrate the potential of remote sensing and satellite Earth Observation (IIWQ, 2018).

References

- Bresciani, M., Giardino, C., Stroppiana, D., Dessena, M.A., Buscarinu, P., Cabras, L., Schenk, K., Heege, T., Bernet, H., Bazdanis, G., Tzimas, A., 2019. Monitoring water quality in two dammed reservoirs from multispectral satellite data. *Eur. J. Remote Sens.* 52, 113–122. <https://doi.org/10.1080/22797254.2019.1686956>
- Bulgarelli, B., D'Alimonte, D., Zibordi, G., Kajiyama, T., 2022. Spectral and atmospheric dependences of the sea-surface reflectance factor in above-water radiometry. In: *Ocean Optics XXV*.
- Bulgarelli, B., Doyle, J.P., 2004. Comparison between numerical models for radiative transfer simulation in the atmosphere-ocean system. *Journal of Quantitative Spectroscopy and Radiative Transfer* 86, 315–334. <https://doi.org/10.1016/j.jqsrt.2003.08.009>
- Bulgarelli, B., Kiselev, V., Zibordi, G., 2014. Simulation and analysis of adjacency effects in coastal waters: a case study. *Applied optics* 53, 1523–1545. <https://doi.org/10.1364/ao.53.001523>
- Bulgarelli, B., Kisselev, V.B., Roberti, L., 1999. Radiative transfer in the atmosphere-ocean system: the finite-element method. *applied optics* 38, 1530–1542. <https://doi.org/10.1364/ao.38.001530>
- Bulgarelli, B., Kisselev, V.B., Roberti, L., 1999. A radiative transfer algorithm for the atmosphere-ocean system based on the finite-element method, in: *IEEE 1999 International Geoscience and Remote Sensing Symposium. IGARSS'99 (Cat. No.99CH36293)*. Geoscience and Remote Sensing Symposium, 1999 IGARSS '99 Proceedings IEEE 1999 International, pp. 1848–1850 vol.3. <https://doi.org/10.1109/igarss.1999.772115>
- Bulgarelli, B., Melin, F., 2000. SeaWiFS data processing code REMBRANDT version 1.0 (REtrieval of Marine Biological Resources through ANalysis of ocean color DaTa) (No. EUR 19514 EN). JRC-EC.
- Bulgarelli, B., Melin, F., Zibordi, G., 2003a. SeaWiFS-derived products in the Baltic Sea: performance analysis of a simple atmospheric correction algorithm. *Oceanologia*.
- Bulgarelli, B., Zibordi, G., 2020. Adjacency radiance around a small island: implications for system vicarious calibrations. *applied optics* 59, C63–C69. <https://doi.org/10.1364/ao.378512>
- Bulgarelli, B., Zibordi, G., 2018a. On the detectability of adjacency effects in ocean color remote sensing of mid-latitude coastal environments by SeaWiFS, MODIS-A, MERIS, OLCI, OLI and MSI. *Remote Sensing of Environment* 209, 423–438. <https://doi.org/10.1016/j.rse.2017.12.021>
- Bulgarelli, B., Zibordi, G., 2018b. Seasonal Impact of Adjacency Effects on Ocean Color Radiometry at the AAOT Validation Site. *Geoscience and Remote Sensing Letters, IEEE* 15, 488–492. <https://doi.org/10.1109/lgrs.2017.2781900>
- Bulgarelli, B., Zibordi, G., 2003. Remote sensing of ocean colour: Accuracy assessment of an approximate atmospheric correction method. *Int. J. of Remote Sensing* 24, 491–509. <https://doi.org/10.1080/01431160304985>
- Bulgarelli, B., Zibordi, G., Berthon, J.-F., 2003b. Measured and modeled radiometric quantities in coastal waters: toward a closure. *Applied optics* 42, 5365–5381. <https://doi.org/10.1364/ao.42.005365>
- Bulgarelli, B., Zibordi, G., Mélin, F., 2018. On the minimization of adjacency effects in SeaWiFS primary data products from coastal areas. *Opt. Express* 26, A709. <https://doi.org/10.1364/oe.26.00a709>

- D'Alimonte, D., Kajiyama, T., Zibordi, G., Bulgarelli, B., 2021. Sea-surface reflectance factor: replicability of computed values. *Opt Express* 29, 25217. <https://doi.org/10.1364/oe.424768>
- Dörnhöfer, K., Klinger, P., Heege, T., Oppelt, N., 2017. Multi-sensor satellite and in situ monitoring of phytoplankton development in a eutrophic-mesotrophic lake. *Science of the Total Environment* 612, 1200–1214. <https://doi.org/10.1016/j.scitotenv.2017.08.219>
- Doyle, J.P., Rief, H., 1998. Photon transport in three-dimensional structures treated by random walk techniques: Monte Carlo benchmark of ocean colour simulations. *Mathematics and Computers in Simulation* 47, 215–241.
- Harrison, A.W., Coombes, C.A., 1988. An opaque cloud cover model of sky short wavelength radiance. *Solar Energy* 41, 387–392. [https://doi.org/10.1016/0038-092x\(88\)90035-7](https://doi.org/10.1016/0038-092x(88)90035-7)
- Hartmann, K., Albada, E., Heege, T., 2021. Latest Developments in Satellite Derived Bathymetry: Technology, Use Cases and Tools. *OCEANS 2021: San Diego - Porto OO*, 1–7. <https://doi.org/10.23919/oceans44145.2021.9706016>
- Heege, T., Kiselev, V., Wettle, M., Hung, N.N., 2014. Operational multi-sensor monitoring of turbidity for the entire Mekong Delta. *Int. J. of Remote Sensing* 35, 2910–2926. <https://doi.org/10.1080/01431161.2014.890300>
- Heege, T., Schenk, K., Wilhelm, M.-L., 2019. Water Quality Information for Africa from Global Satellite Based Measurements: The Concept Behind the UNESCO World Water Quality Portal, in: Froehlich, A. (Ed.), *Embedding Space in African Society, Southern Space Studies*. Springer, pp. 81–92. https://doi.org/10.1007/978-3-030-06040-4_5
- Heney, L.G., Greenstein, J.L., 1941, Diffuse radiation in the galaxy. *Astrophysical Journal* 93, 70-83
- IIWQ, 2018. The UNESCO - IHP IIWQ World Water Quality Portal - Whitepaper.
- Kajiyama, T., D'Alimonte, D., Bulgarelli, B., Mazeran, C., Liberti, G., 2022. SHADING EFFECTS INDUCED BY OPTICAL BUOYS FOR SYSTEM VICARIOUS CALIBRATION, in: *Ocean Optics XXV*.
- Kajiyama, T., Zibordi, G., Bulgarelli, B., Talone, M., D'Alimonte, D., 2024, Radiative transfer simulations of water-leaving radiance from the Skylight-Blocked Approach. Submitted to *Optics Express*.
- Kiselev, V., Bulgarelli, B., Heege, T., 2015. Sensor independent adjacency correction algorithm for coastal and inland water systems. *Remote Sensing of Environment* 157, 85–95. <https://doi.org/10.1016/j.rse.2014.07.025>
- Kisselev, V.B., Roberti, L., Perona, G., 1995. Finite-element algorithm for radiative transfer in vertically inhomogeneous media: numerical scheme and applications 34, 8460–8471.
- Kneizys, F.X., Shettle, E.P., Abreu, L.W., Chetwynd, J.H., Anderson, G.P., 1988. Users Guide to LOWTRAN 7.
- Liou, K.-N., 2002. *An Introduction to Atmospheric Radiation*, Academic Press. Academic Press.
- Mélin, F., Clerici, M., Zibordi, G., Bulgarelli, B., 2006. Aerosol variability in the Adriatic Sea from automated optical field measurements and Sea-viewing Wide Field-of-view Sensor (SeaWiFS). *Journal of Geophysical Research: Atmospheres* 111, D22201. <https://doi.org/10.1029/2006jd007226>
- Mobley, C.D., 1999. Estimation of the remote-sensing reflectance from above-surface measurements. *applied optics* 38, 7442–7455. <https://doi.org/10.1364/ao.38.007442>
- Mobley, C.D., 1994. *Light and water: Radiative transfer in natural waters*. Academic press San Diego 592.

- Mobley, C.D., Gentili, B., Gordon, H.R., Jin, Z., Kattawar, G.W., Morel, A., Reinersman, P., Stamnes, K., Stavn, R.H., 1993. Comparison of numerical models for computing underwater light fields. *Applied Optics* 32, 7484–7504.
- Monahan, E.C., O’Muircheartaigh, I.G., 1986. Whitecaps and the passive remote sensing of the ocean surface. *Int. J. of Remote Sensing* 7, 627–642. <https://doi.org/10.1080/01431168608954716>
- Petzold, T.J., 1972. Volume scattering functions for selected ocean waters (No. SIO Ref. 72-78). University Of California, San Diego Scripps Institution Of Oceanography Visibility Laboratory San Diego, California 92152.
- Riha, S., Krawczyk, H., 2013. Remote Sensing Of Cyanobacteria And Green Algae In The Baltic Sea, in: ASPRS Annual Conference. Baltimora, Maryland.
- Roberti, L., 1997. Monte Carlo radiative transfer in the microwave and in the visible: biasing techniques. *Applied Optics*, 36, 7929–7938.
- Saltelli, A., Bammer, G., Bruno, I., Charters, E., Fiore, M.D., Didier, E., Espeland, W.N., Kay, J., Piano, S.L., Mayo, D., Pielke, R., Portaluri, T., Porter, T.M., Puy, A., Rafols, I., Ravetz, J.R., Reinert, E., Sarewitz, D., Stark, P.B., Stirling, A., Sluijs, J. van der, Vineis, P., 2020. Five ways to ensure that models serve society: a manifesto. 482–484.
- Storch, T., Honold, H.-P., Chabrillat, S., Habermeyer, M., Tucker, P., Brell, M., Ohndorf, A., Wirth, K., Betz, M., Kuchler, M., Mühle, H., Carmona, E., Baur, S., Mücke, M., Löw, S., Schulze, D., Zimmermann, S., Lenzen, C., Wiesner, S., Aida, S., Kahle, R., Willburger, P., Hartung, S., Dietrich, D., Plesia, N., Tegler, M., Schork, K., Alonso, K., Marshall, D., Gerasch, B., Schwind, P., Pato, M., Schneider, M., Reyes, R. de los, Langheinrich, M., Wenzel, J., Bachmann, M., Holzwarth, S., Pinnel, N., Guanter, L., Segl, K., Scheffler, D., Foerster, S., Bohn, N., Bracher, A., Soppa, M.A., Gascon, F., Green, R., Kokaly, R., Moreno, J., Ong, C., Sornig, M., Wernitz, R., Bagschik, K., Reintsema, D., Porta, L.L., Schickling, A., Fischer, S., 2023. The EnMAP imaging spectroscopy mission towards operations. *Remote. Sens. Environ.* 294, 113632. <https://doi.org/10.1016/j.rse.2023.113632>
- Zibordi, G., Berthon, J.F., Doyle, J.P., Grossi, S., Linde, D. van der, Targa, C., Alberotanza, L., 2002. Coastal Atmosphere and Sea Time Series (CoASTS), Part 1: A tower-based, long-term measurement program. NASA Technical Memorandum - SeaWiFS Postlaunch Technical Report Series 1–29.
- Zibordi, G., Bulgarelli, B., 2007. Effects of cosine error in irradiance measurements from field ocean color radiometers. *applied optics* 46, 5529–5538. <https://doi.org/10.1364/ao.46.005529>
- Zibordi, G., Holben, B., Mélin, F., D’Alimonte, D., Berthon, J.F., Slutsker, I., Giles, D., 2010. AERONET-OC: an overview. *Canadian Journal of Remote Sensing* 36, 488–497. <https://doi.org/10.5589/m10-073>
- Zibordi, G., Mélin, F., Berthon, J.-F., Holben, B., Slutsker, I., Giles, D., D’Alimonte, D., Vandemark, D., Feng, H., Schuster, G., Fabbri, B.E., Kaitala, S., Seppälä, J., 2009. AERONET-OC: A Network for the Validation of Ocean Color Primary Products. *J Atmos Ocean Tech* 26, 1634–1651. <https://doi.org/10.1175/2009jtecho654.1>
- Zibordi, G., Voss, K.J., 1989. Geometrical and spectral distribution of sky radiance - Comparison between simulations and field measurements. *Remote Sensing of Environment (ISSN 0034-4257)* 27, 343–358. [https://doi.org/10.1016/0034-4257\(89\)90094-1](https://doi.org/10.1016/0034-4257(89)90094-1)

List of abbreviations and definitions

AC	Atmospheric Correction
AE	Adjacency Effects
AERONET-OC	Ocean Color component of the Aerosol Robotic Network
AOPs	Apparent Optical Properties
AquaFEM	FEM configuration for the simulation of the in-water light field
ARTEMIS-OC	Advanced Radiative Transfer Models for In Situ and Satellite Ocean Color data
C3S	Climate Change Service
CMEMS	Copernicus Marine Environment Monitoring Service
ECV	Essential Climate Variable
EO	Earth Observation
EOSS	Earth Observation Support to Copernicus Climate and Marine Services
EU	European Union
DLR	German Aerospace Center
EnMAP	Environmental Mapping and Analysis Program
EUMETSAT	European Organization for the Exploitation of Meteorological Satellites
FEM	Finite Element Method code
FEMrad-OC	FEM configuration for the simulation of the radiance at Ocean Color satellite sensors
GCOS	Global Climate Observation System
GOOS	Global Ocean Observing System
HC	Harrison and Coombs parameterization
IIWQ	International Initiative on Water Quality
IOPs	Inherent Optical Properties
JRC	Joint Research Centre
LOWTRAN	Low Resolution Transmission Model
MC	Monte Carlo
MC-R	Roberti's MC code
MERIS	Medium Resolution Imaging Spectrometer
MIP	Modular Inversion and Processing System
NASA	National Aeronautics and Space Administration
NAUSICAA	Novel Adjacency Perturbation Simulator for Coastal Areas
NIR	Near Infrared
OC	Ocean Color
OLCI	Ocean and Land Colour Instrument
PHO-TRAN	
RE	Relative Error
RTE	radiative transfer equation
RTM	radiative transfer model
SeaWiFS	Sea Wide Field of View Sensor
SkyFEM	FEM configuration for the simulation of the Sky-radiance
SVC	System Vicarious Calibration
TOA	Top of Atmosphere
UNESCO	United Nations Educational, Scientific and Cultural Organization
UNFCCC	United Nations Framework Convention on Climate Change
ZV	Zibordi and Voss parameterization

List of figures

Figure 1. Scheme of a RTM, as composed by a core algorithm for the mathematical solution of the RTE and a parametric modelling of the propagating system.....	7
Figure 2. ARTEMIS-OC modelling capabilities.....	8
Figure 3. Scheme of the FEM code for the solution of the RTE.....	9
Figure 4. Scheme for the modelling of the propagating system.....	10
Figure 5. Scheme for SkyFEM, FEMrad-OC and AquaFEM	10
Figure 6. Scheme for NAUSICAA.....	11
Figure 7. Illustration of a solid angle and its representation in polar coordinates. Also shown is a pencil of radiation through an element of area dA in directions confined to an element solid angle $d\Omega$	13
Figure 8. Example of MAIN.DAT input file.	17
Figure 9. Scheme of the atmosphere-ocean system	17
Figure 10. Example of input file defining the characteristics of the propagating medium (e.g., <i>card1.dat</i>).....	18
Figure 11. Example of input file containing the Legendre moments of the phase function (e.g., <i>momname.dat</i>).....	19
Figure 12. Example of input file defining the output characteristics (e.g., <i>card2.dat</i>).....	19
Figure 13. the Applied reference geometry: $\eta_0 = \cos\theta_0$; $\eta = \cos\theta$; $\Delta\phi$ is the radiance azimuth with respect to the sun-beam azimuth. Zenith angles are computed with respect to the τ axis.	20
Figure 14. Example of uncommented output file (e.g., <i>ofname.dat</i>)	21
Figure 15. Example of verbose output file (e.g., <i>ofname.out</i>)	22
Figure 16. Radiance [$\text{Wm}^{-2} \text{nm}^{-1} \text{sr}^{-1}$] simulated with FEM($N=64$) just above the air–water interface. Empty circles indicate results obtained with MC-R (Roberti, 1997) initializing 10^6 photons.....	26
Figure 17. Radiance [$\text{Wm}^{-2} \text{nm}^{-1} \text{sr}^{-1}$] simulated with FEM($N=64$) just below the air–water interface. Empty circles indicate results obtained with MC-R (Roberti, 1997) with 10^6 photons.	26
Figure 18. Intercomparison between (–) FEM($N=64$) and (•) PHO-TRAN(10^5 photons) simulated values for problem 3 ($\theta_0=45^\circ$, $\Phi_0=0^\circ$, $E_0=1 \text{ W m}^{-2} \text{nm}^{-1}$). The radiance angular distributions [$\text{Wm}^{-2} \text{nm}^{-1} \text{sr}^{-1}$] is displayed on the left panels, while the relative percentage differences, with bars representing the 99% confidence on the PHO-TRAN results, are shown on the right panels. The upper panels (a) display results just above the water surface, while the lower panels (b) show results just beneath the water surface. The symbols θ_v and Φ_v indicate the viewing direction with $\theta=180^\circ-\theta_v$ and $\Phi=180^\circ+\Phi_v$. $0^\circ<\theta_v<90^\circ$ indicates to down-looking directions while $90^\circ<\theta_v<180^\circ$ refers to the up-looking directions.	27
Figure 19. Intercomparison between (x) FEM($N=64$) and (•) PHO-TRAN(10^5 photons) simulations for the realistic problem. Panels (a) display in-water profiles of nadir Lu [$\text{W m}^{-2} \text{nm}^{-1} \text{sr}^{-1}$], Ed and Eu [$\text{Wm}^{-2} \text{nm}^{-1}$] while panels (b) illustrate the correspondent relative differences. Bars represent the 99% confidence on PHO-TRAN results.	28
Figure 20. Normalized distributions of $\delta_{\text{MC-FEM}} E_0 = (L_{\text{MC}} - L_{\text{FEM}}) / E_0$ [sr^{-1}] over 672 test cases between TOA radiances computed with FEM($N=64$) and NAUSICAA (10^7 photons) assuming (a) a uniform ideal Lambertian surface and (b) a uniform Fresnel-reflecting surface. The Gaussian fit of the distributions is displayed in black. Its mean $\langle \delta E_0 \rangle$ and standard deviation $\sigma_\delta E_0$ are also given. Note that the scale for the Lambertian case is one order of magnitude higher than that of the Fresnel case.....	28
Figure 21. In-water profiles of Lu , Eu and Ed at 665 nm (normalized to the subsurface downward irradiance) simulated with (red circles) FEM and with (blue circles) Hydrolight 4.1.....	29
Figure 22. In-water profiles of relative differences $\epsilon(L_u)$, $\epsilon(E_u)$, and $\epsilon(E_d)$ at (blue) 412, (red) 490, and (green) 555 nm between experimental and FEM theoretical data: $\epsilon(x) = 100 \cdot (x_{\text{FEM}} / x_{\text{exp}} - 1)$. The dotted lines delimit the $\pm 10\%$ and $\pm 20\%$ regions.	29

Figure 23. Scheme of the MIP modules for water-quality processing	31
Figure 24. Relative difference between theoretical and experimental <i>Ed</i> data just above the water surface for representative experimental test-cases.....	32
Figure 25. Partitioning of the upper hemisphere into quads. The thick solid and dashed lines indicate the measurement and the solar plane, respectively. The sensor-quad marked in black represents the virtual radiometer.....	32
Figure 26. Example of diffuse sky-radiance distributions at 550 nm obtained with FEM(N=64) for $\theta_0 = 20^\circ$, 40° and 60°	33
Figure 27. Diffuse sky radiance <i>Lsky</i> at 550 nm determined for the solar and measurement planes (solid and dashed lines, respectively) with HC, ZV and FEM for different θ_0 (i.e., 20° , 40° and 60°).	33

List of tables

Table 1. mean and absolute Relative Error (RE) between FEM(N=4) and FEM (N=64) values computed at TOA over 209 viewing angles with $\theta_0=45^\circ$ for sample test cases	24
Table 2. Average Values of E_d , E_{0u} , and L_u at selected depths from Mobley et al., (1993) for Problem 3 with their sample standard deviation, and corresponding values obtained with FEM (N=4) and FEM (N= 64)	25
Table A.1. Structure of the MAIN.DAT	43
Table A.2. Structure of the input file defining the propagating system.....	44
Table A.4. Structure of the input file containing the Legendre coefficients of the scattering phase function ..	47
Table A.5. FEM parameters definition and default values.....	50
Table A.6. FINWAT.FOR variables.....	51

Annexes

Annex 1. Code Structure

The FEM code consists of the following Fortran routines:

FEMWAT.FOR

it is the main programme that reads the input data files, calls the main subroutine FINWAT, and writes the output data files

FINWAT.FOR

it is the main subroutine that checks the consistency of the input data and sums up the radiance harmonics estimated by subsequent calls to the subroutine HARMWAT.

HARMWAT.FOR

it estimates the radiance harmonics

SUBWAT.FOR

it contains subroutines for the solution of the linear algebraic system and for the interpolation the solution

WSURF.FOR

it computes the matrices defining the boundary conditions at the air-water interface

SUBLIB.FOR

it contains linked subroutines from the SLATEC, BLAS and LAPACK public domain FORTRAN libraries

Annex 2. Input-files format

The structure of the input files is outlined in Table A.1 to A.4.

All the files include header and separator lines, which are intended for user comments and whose content may be arbitrary. Nonetheless, they must be necessarily defined in the file. The last line of each file must contain the CARRIAGE RETURN symbol in the end (simply press ENTER key when editing).

The leading input file, named MAIN.DAT, must be located in the directory of the executable module. The name of the file MAIN.DAT must not be changed. Name and location of the other files can be defined by the user specifying the complete path in the file MAIN.DAT.

Table A.1. Structure of the MAIN.DAT

Lines 1-3	Header (arbitrary text, not used by the program)
Line 4	name of the input file defining the propagating system (e.g., <i>card1.dat</i>) <code>format (27x,a)</code>
Line 5	name of the input file defining the output characteristics (e.g., <i>card2.dat</i>) <code>format (27x,a)</code>
Line 6	name of the output-file, where output data are stored without comments (e.g., <i>ofname.dat</i>) <code>format (27x,a)</code>
Line 7	name of the verbose output file, where output data are stored together with comments and input data (e.g., <i>ofname.out</i>) <code>format (27x,a)</code>
Line 8	flag HENYEY to select phase functions type (valid for all layers): if HENYEY = 1, TTHG phase functions are selected for each layer if HENYEY = 0, layers phase functions are ingested from the file defined

	at Line 9 <code>format (27x,i1)</code>
Line 9 (necessary only if phase functions are not approximated as TTHG)	name of the containing for each layer the Legendre coefficients of the phase function (e.g., <i>momname.dat</i>) <code>format (27x,a)</code>

Table A.2. Structure of the input file defining the propagating system (e.g., *card1.dat*)

Lines 1-3	Header (arbitrary text, not used by the program)
Line 4	Number N of grid points for the half-interval of the angular variable (see eq. 15). This parameter defines the accuracy of the computation (see Section 3.3) <code>format (49x,i3)</code>
Lines 5-6	separators
Line 7	Solar zenith angle [deg] and solar irradiance at TOA. The solar zenith angle is the angle between the incident beam direction and the normal to the surface (see Fig. 9). The solar irradiance at TOA is the solar spectral irradiance <u>on a surface normal to the solar beam direction</u> <code>format (7x,f8.5,17x,f16.11)</code>
Lines 8-9	separators
Line 10	surface albedo and surface asymmetry factor (HG bi-directional reflectance with asymmetry factor <i>g</i>) NOTA: <u>the asymmetry factor equals 0.0 for Lambertian surfaces</u> <code>format (34x,f6.5,10x,f6.5)</code>
Lines 11-12	separators
Line 13	number <i>nlatm</i> of horizontal layers in which the atmosphere is divided and atmosphere refractive index (N.B. at least one atmospheric layer must be present in the system). <code>format (34x,i2,15x,f7.5)</code>
Line 14	number <i>nlatm</i> of horizontal layers in which the water is divided and water refractive index (N.B. if no water layers are included <i>nlatm</i> must be set to 0). <code>format (34x,i2,15x,f7.5)</code>
Line 15-17	separators
<i>nlatm</i> + <i>nlatm</i> lines follow, each of	- layer number (<u>layers are numbered from TOA in increasing order, see Fig. 9</u>)

which contains:	<ul style="list-style-type: none"> - single scattering albedo (ssa) - layer optical thickness (tau) <pre>format (11x,i2,11x,f11.9,5x,f13.9)</pre>
Lines 18+ <i>nlatm</i> + <i>nlwat</i> -20+ <i>nlatm</i> + <i>nlwat</i>	separators
If TTHG phase functions, <i>nlatm</i> + <i>nlwat</i> lines follow, each of which contains:	<ul style="list-style-type: none"> - layer number (<u>layers are numbered starting from TOA in increasing order, see Fig. 9</u>) - TTHG forward asymmetry factor (g_1) - TTHG backward asymmetry factor (g_2): <u>positive</u>. - TTHG forward-to-backward weight (as) <p>NOTE1: If the phase functions are not of TTHG type (i.e., HENYEY=0) these lines are not read.</p> <p>NOTE2: If single-term HG phase functions are used:</p> <p>$g_2 = 0.d0$ and $as = 1.d0$</p> <pre>format (11x,i2,11x,f11.9,7x,f11.9,7x,f11.9)</pre>

Table A.3. Structure of the input file defining the output characteristics (e.g., *card2.dat*)

Lines 1-3	Header (arbitrary text, not used by the program)
Line 4	<p>flag <i>radiance</i> to select the computation of the radiance L or of a radiance harmonic L_m (see Eq. 13)</p> <p>= 1: radiance/radiance harmonic is computed</p> <p>= 0: otherwise</p> <pre>format (35x,i1)</pre>
Line 5	<p>flag <i>irrad</i> to select the computation of the irradiance E (see Eq. 5)</p> <p>= 1: the irradiance is computed</p> <p>= 0: otherwise</p> <pre>format (35x,i1)</pre>
Line 6	separator
Line 7	<p>number <i>m</i> of the radiance harmonics L_m (see Eq. 13) to be computed</p> <p><u>if $m = -1$ the radiance L is computed</u></p> <p>If at Line 4 <i>radiance</i> = 0, this parameter is of no importance (but must be present in the input)</p> <pre>format (49x,i3)</pre>
Line 8	<p>number <i>nt</i> of levels at which the solution is computed</p> <pre>format (49x,i3)</pre>

<i>nt</i> lines follow, each of which contains	the computational optical thicknesses; optical thicknesses must follow one another <u>in increasing order</u> . <u>NOTE: the optical thickness is computed starting from TOA (see Fig. 9)</u> free format
Line 9+ <i>nt</i>	number <i>naz</i> of computational azimuth angles; format (49x, i3)
<i>naz</i> lines follow, each of which contains	the computational azimuth angle in degrees <u>in increasing order</u> . <u>NOTE: computational azimuth angles are determined with respect to the azimuth of the incident solar beam (see Fig.13).</u> free format
Lines 10+ <i>nt</i> + <i>naz</i>	number <i>nang</i> of computational polar angles; format (49x, i3)
Lines 11+ <i>nt</i> + <i>naz</i>	Flag <i>equi</i> If <i>equi</i> = 1 <i>nang</i> computational cosines of the polar angles, homogeneously distributed in the interval [-1,1], are assumed; If <i>equi</i> = 0 the <i>nang</i> computational cosines of the polar angles are read from the following <i>nang</i> lines format (51x, i1)
<i>nang</i> lines follow (if <i>equi</i> = 0, otherwise not read), each of which contains	the cosine of the computational polar angle <u>in increasing order</u> . <u>NOTE: computational polar angles are computed with respect to the τ axis: positive cosines correspond to downgoing radiance; negative cosines to upgoing radiance (see Fig. 13).</u> free format

When the phase functions are not approximated as TTHG, the user must provide a file containing the coefficients (moments) of the phase function expansion in a Legendre series (Eq. 9). The moment number 1 is the coefficient of the Legendre polynomial of 0th degree, the moment number 2 is the coefficient of the Legendre polynomial of 1st degree, etc. The file is unformatted and consists of *nI* blocks of lines (one block for each layer).

Notably, the phase functions must be normalized to 4π , so that moment number 1, x_1 , is equal to 1.

Indeed

$$\int_{\Omega} \tilde{\beta}(\Theta) d\Theta = \int_0^{2\pi} d\phi \int_{-1}^1 \tilde{\beta}(\eta) d\eta = 4\pi \quad (18)$$

requires

$$\int_{-1}^1 \tilde{\beta}(\eta) d\eta = 2 \quad (19)$$

and hence

$$x_1 = \frac{1}{2} \int_{-1}^1 \tilde{\beta}(\eta) d\eta = 1 \quad (20)$$

Table A.4. Structure of the input file containing the Legendre coefficients of the scattering phase function (e.g., *momname.dat*)

Lines 1	number of the layer <i>nnl</i> and number of the moments <i>nmom</i> for the layer (maximum value of <i>nmom</i> is the NMX parameter)
Line 2 – 1+ <i>nmom</i>	number of the moment and its value

Annex 3. Output-files format

FEM provides highly accurate angular distributions of the diffuse radiance, as well as direct and diffuse irradiances at any location of the propagating system.

The program creates two output files: a “computer-oriented” file (e.g., *ofname.dat*), which contains only unformatted and uncommented output results considered convenient for further computations or visualizations; and a “human-oriented” file (e.g., *ofname.out*) where output data are accompanied by comments and input data.

The structure of uncommented output data (e.g., *ofname.dat*) is the following:

If the radiance is computed:

```
<tau value>
<Azimuthal angle value>
<cosine value>      <radiance value>
.....
.....
<cosine value>      <radiance value>
```

If a specific harmonic is computed then:

```
<harmonic number>
<tau value>
<cosine value>      <harmonic value>
.....
.....
.....
```

The structure of the verbose output data (e.g., *ofname.out*) is the following:

```
Spectral Irradiance=<value>
Solar zenith angle (deg)= <value>
Surface albedo = <value>
Surface asymmetry factor = <value>
Number of grid points for half interval = <value>
-----
Refractive Index
-----
Atmospheric Layers <# atm lay.> <n(atm) value>
Water Layers      <# wat lay. > <n(wat) value>
-----

Layers characteristics:
```

<i>nl</i>	<i>ssa</i>	<i>Tau-tot</i>
<layer number>	<LAMBDA value>	<TAU value>
.....
.....
.....

N.B. the Tau-tot values listed above are computed from the top of the atmosphere down to the layer's lower boundary

If the phase function is not Henyey-Greenstein then:

Henyey-Greenstein = .false.
phase function file= <name>

If the phase function is Henyey-Greenstein then:

Henyey-Greenstein = .true.

<i>nl</i>	<i>g1</i>	<i>g2</i>	<i>as</i>
<layer number>	<g1 value>	<g2 value>	<as value>
.....
.....

If the radiance is computed

RADIANCE
tau = <tau value>
azimuth = <Azimuthal angle value>
cos(polar angle) *Radiance Value*
<cosine value> <Radiance value>
.....
.....
.....

If a specific harmonic is computed then:

Harmonic number = <harmonic number>
tau = <tau value>
cos(polar angle) *harmonic value*
<cosine value> <Harmonic value>
.....
.....
.....

If the irradiance is computed then:

Irradiance
tau = <tau value>
Upgoing diffuse irradiance = <.....>
Dowgoing diffuse irradiance= <.....>
\$ Downgoing direct irradiance= <.....> \$
\$ Reflected direct irradiance= <.....> \$
@ Transmitted direct irradiance= <.....> @

$$TOTAL\ IRRADIANCE = <.....>$$

\$ (only for atmospheric layers)
 @ (only for water layers)

Annex 4. Accuracy of the solution

As anticipated in Section 3.3, the accuracy of the radiance solution is determined by

- parameter ϵ (variable EPSI in FEMWAT.FOR and FINWAT.FOR). if $L^m \leq \epsilon$ the radiance Fourier series of Eq. 13 is truncated.
- the number of grid points N defining through Eq. 15 the accuracy of each computed radiance harmonics L^m .

Although EPSI and N are formally independent, since the overall accuracy is determined by the lowest of the two parameters, the optimal balance between accuracy and CPU time consumption is obtained when EPSI and the accuracy in the computation of L^m are of the same order of magnitude.

EPSI is a hard-coded variable defined in the FEMWAT.FOR at "*Setting the accuracy of harmonics summation*". EPSI is set by default to 1.d-4, but can be arbitrarily changed by the user [NOTE: if the computation of a radiance harmonic is selected (hence $m > 0$), EPSI must be negative]. EPSI increase will clearly result in larger CPU time. It is noticed that:

- EPSI refers to the absolute accuracy of the diffuse radiance. Direct, reflected and refracted radiances (see Section 3.2) are always estimated with computer arithmetic accuracy, which is the highest possible for the computing system.
- EPSI is an absolute accuracy of the radiance for a unit solar flux, and not for the spectral irradiance defined by the user in the input data.
- The maximum number of harmonics, which is further compared with the required L^m accuracy, refers to all computational angles and optical depths.

The accuracy in the computation of each radiance harmonic L^m is controlled by the number of grid points N, which is an input variable (see 3.2). The higher the number of grid points, the higher is L^m accuracy. The number of grid points must be chosen by the user with a *try-and-see* method. It is meaningful to increase N only until this leads to a variation in the solution that is higher than EPSI.

In typical cases the accuracy 1.d-4 (EPSI default value) is reached with 6-8 grid points, but it greatly depends on the phase functions and the output geometry. For highly peaked phase functions, especially if the radiances below the air-water interface are required, only 16 or even more grid points ensure the desired accuracy. The simulation of the downgoing radiance originating around the solar beam might require up to 64 grid points.

The accuracy of the irradiance computations solely depends on N and it is regularly higher than the radiance accuracy. For example, N = 2 is generally sufficient for an irradiance accuracy in the order of 1.d-3; N = 4 typically guarantees an accuracy in the order of 1.d-4.

Annex 5. Compilation and linking

The executable module is created by compiling and linking the FORTRAN files listed in Section A.1.

In order to execute the program, the MAIN.DAT input file must be in the same directory of the executable file.

The file SUBLIB.FOR contains a subroutine for the determination of machine-dependent parameters for local machine environments (INTEGER FUNCTION I1MACH(I) at line 1160), which must be therefore adapted to the specific computer. To alter this function for a particular environment, the desired set of DATA statements, listed in the subroutine, should be activated by removing the C from column 1. Also, the values of I1MACH(1) - I1MACH(4) should be checked for consistency with the local operating system.

If during the execution problems arise, error messages appear on the screen, together with the result flag IRES:

IRES = 1 : a contradiction in the input parameter has occurred, but the program tried to solve it after informing the user.

IRES = 2 : both harmonic number and accuracy are positive, the priority is given to harmonic number.

IRES = -1 : the problem cannot be solved due to serious contradictions in the parameter set.

For more details on error messages see FINWAT.FOR

The FEM code was developed on a VAX 7000 with VMS operative system. Since then it has been run faultless on Unix, DOS and iOS systems.

Annex 6. Program Parameters

Program parameters set the maximum dimension of the arrays defining the input and output data, which can be processed in a single program run. They hence define the amount of core memory necessary for the program execution.

The necessary amount of memory is defined mainly by the size of the arrays for the data storage. Notably, the default values listed in Table A.5, can be substituted by other values, if necessary.

Table A.5. FEM parameters definition and default values

Parameter Name	Meaning	Default Value
MLAY	Maximum number of layers	32
NMPT	Maximum number of grid points in half of the interval of the cosine of the polar angle	64
NMANG	Maximum number of zenith angles for the computation of the solution in the total interval $[-1,1]$ for the correspondent cosines).	150
NMAZ	Maximum number of azimuthal angles for the computation of the solution in the total interval $[-\pi,\pi]$.	16
NMT	Maximum number of levels for the computation of the solution	10
NMX	Maximum number of Legendre moments of the phase function expansion (for each layer)	1600

Annex 7. Program Main Variables

The main subroutine is FINWAT.FOR, whose input/output variables are detailed in Table A.6

Table A.6. FINWAT.FOR variables

INPUT PARAMETERS		
Description of the propagating medium		
ZZ	R*8	Cosine of the incident beam polar angle, positive between [0,1]. The incident beam azimuthal angle is 0.
SOCO	R*8	Intensity of the incident parallel beam on the top boundary in arbitrary units. It is such that $n \cdot \text{SOCO} = \text{incident flux}$.
ALBEDO	R*8	The surface albedo.
NCSUR	I	The number of coefficients in the Legendre expansion of the surface reflection coefficient
XSUR	R*8	Array of dimension at least NCSUR containing the coefficients of the Legendre expansion of the surface reflection coefficient. If the surface is Lambertian then $\text{XSUR}(1)=1$; $\text{NCSUR}=1$
NL	I	Number of layers ($\text{NL} \leq \text{NMLAY}$) Layers are numbered starting from the top boundary down.
NW	I	Index of the first water layer ($\text{NW} < \text{NL}$)
ARI	R*8	Air relative refractive index
WRI	R*8	Water relative refractive index
TAUO	R*8	Array of dimension at least NL containing, for each layer, the total optical depth, i.e., the optical depth measured from the top boundary of the medium to the lower boundary of the layer itself.
LAMBDA	R*8	Array of dimension at least NL containing the single scattering albedo for each layer.
NC	I	Array of dimension at least NL containing the number of coefficients in the Legendre expansion of the phase function for each layer.
XCOF	R*8	Array of dimension ($\text{NMX}, *$). The second dimension must be at least NL. $\text{XCOF}(*, \text{I})$ contains the coefficients of the Legendre expansion of the phase function for the I-th layer. The moment of order 1 must be equal to 1.
NMX	I	The first dimension of the array XCOF. Must be at least equal to the maximum value in NC.
definition of the output solution		
RADIANCE	I	Flag: =1 the radiance (the radiance harmonic) is computed =0 otherwise
IRRAD	I	Flag: =1 the irradiance is computed =0 otherwise
NT	I	Number of computational levels ($\text{NT} \leq \text{NMT}$)
TAUE	R*8	Array of dimension at least NT containing the computational levels in increasing order between 0 and the total optical thickness of the medium.
NAZ	I	Number of computational azimuthal angles ($\text{NAZ} \leq \text{NMAZ}$)
AZE	R*8	Array of dimension at least NAZ. Computational azimuthal angles in increasing order between [0,180]
NANG	I	Number of computational polar angles ($\text{NANG} \leq \text{NMANG}$)
ANG	R*8	Array of dimension at least NANG containing the cosines of computational polar angles in increasing order between [-1,1]. NB: Positive cosines denote downgoing radiation. Negative cosines denote upgoing radiation
Computational requirements		
NHARM	I	Number of the Fourier harmonic of the radiance to be estimated. If the radiance is needed, then NHARM must be set to -1.

N	I	Number of grid-points for half of the interval of the polar angle. (Critical for computational time) ($N \leq NMPT$). The accuracy of the harmonics estimate depends on the value of N.
EPSI	R*8	The ACCURACY for the RADIANCE computation. In the radiance computation, if the maximum value of the computed harmonic over all the computational angles and layers is below this threshold the summation over the harmonics ends. It influences the CPU time. EPSI=1.E-4 is adopted for N=16,32. If N=2,4 grid-points are used EPSI=1.E-3 is more recommended. <u>EPSI must be set to a negative value if only one harmonic is to be estimated.</u>
OUTPUT PARAMETERS		
INTEN	R*8	Array of dimension (NMXT,NMXZ,*) containing the solution. The third dimension must be at least NANG. The measure units are those of SOCO.
NMXT	I	The first dimension of the array INTEN ($\geq NT$)
NMXZ	I	The second dimension of the array INTEN ($\geq NAZ$)
RFCOF	R*8	Solar beam reflection coefficient.
TRCOF	R*8	Solar beam transmission coefficient, relative to a normal surface.
ANGF	R*8	Array of dimension at least NANG containing the cosines of refracted computational polar angles in increasing order between [-1,1].
ZZW	R*8	Cosine of the refracted beam polar angle, positive between [0,1]. The incident beam azimuthal angle is 0.
ETALIM	R*8	Critical angle, beyond which there is total internal reflection.
FLUXUP	R*8	Array containing the upward diffuse irradiance
FLUXDOWN	R*8	Array containing the downward diffuse irradiance
IRES	I	Result flag. = 0 normal execution. = 1 a contradiction in the input parameter has occurred, the radiance is not computed for some parameters' values. = 2 the estimate of the radiance is suppressed by the request to compute a single radiance harmonic. =3 the surface albedo was corrected =-1 the problem cannot be solved due to serious contradictions in the parameter set. For more details on error messages see FINWAT.FOR

GETTING IN TOUCH WITH THE EU

In person

All over the European Union there are hundreds of Europe Direct centres. You can find the address of the centre nearest you online (european-union.europa.eu/contact-eu/meet-us_en).

On the phone or in writing

Europe Direct is a service that answers your questions about the European Union. You can contact this service:

- by freephone: 00 800 6 7 8 9 10 11 (certain operators may charge for these calls),
- at the following standard number: +32 22999696,
- via the following form: european-union.europa.eu/contact-eu/write-us_en.

FINDING INFORMATION ABOUT THE EU

Online

Information about the European Union in all the official languages of the EU is available on the Europa website (european-union.europa.eu).

EU publications

You can view or order EU publications at op.europa.eu/en/publications. Multiple copies of free publications can be obtained by contacting Europe Direct or your local documentation centre (european-union.europa.eu/contact-eu/meet-us_en).

EU law and related documents

For access to legal information from the EU, including all EU law since 1951 in all the official language versions, go to EUR-Lex (eur-lex.europa.eu).

Open data from the EU

The portal data.europa.eu provides access to open datasets from the EU institutions, bodies and agencies. These can be downloaded and reused for free, for both commercial and non-commercial purposes. The portal also provides access to a wealth of datasets from European countries.

Science for policy

The Joint Research Centre (JRC) provides independent, evidence-based knowledge and science, supporting EU policies to positively impact society



EU Science Hub

joint-research-centre.ec.europa.eu



Publications Office
of the European Union